Diurnal variations in the stratosphere of an ultrahot exoplanet

Thomas Mikal-Evans (tmevans@mpia.de)
Max Planck Institut fur Astronomie

David Sing
Johns Hopkins University https://orcid.org/0000-0001-6050-7645

Joanna Barstow
The Open University

Tiffany Kataria
Jet Propulsion Laboratory, California Institute of Technology

Jayesh Goyal
Cornell University

Nikole Lewis
Cornell University

Jake Taylor
University of Oxford

Nathan Mayne
University of Exeter https://orcid.org/0000-0001-6707-4563

Tansu Daylan
Massachusetts Institute of Technology

Hannah Wakeford
University of Bristol

Mark Marley
Univ. of Arizona https://orcid.org/0000-0002-5251-2943

Jessica Spake
California Institute of Technology

Article

Keywords: exoplanets, WASP-121b, spectroscopic phase curve

Posted Date: November 23rd, 2021

DOI: https://doi.org/10.21203/rs.3.rs-108192/v1

Version of Record: A version of this preprint was published at Nature Astronomy on February 21st, 2022.
See the published version at https://doi.org/10.1038/s41550-021-01592-w.

Diurnal variations in the stratosphere of an ultrahot exoplanet

Thomas Mikal-Evans[1,2] *, David K. Sing[3,4], Joanna K. Barstow[5], Tiffany Kataria[6], Jayesh Goyal[7,8], Nikole Lewis[7], Jake Taylor[9,10], Nathan. J. Mayne[11], Tansu Daylan[2,12], Hannah R. Wakeford[13], Mark S. Marley[14], Jessica J. Spake[15]

[1]Max-Planck-Institut für Astronomie, Heidelberg, Germany. [2]Kavli Institute for Astrophysics and Space Research, Massachusetts Institute of Technology, Cambridge, MA, USA. [3]Department of Earth & Planetary Sciences, Johns Hopkins University, Baltimore, MD, USA. [4]Department of Physics & Astronomy, Johns Hopkins University, Baltimore, MD, USA. [5]School of Physical Sciences, The Open University, Milton Keynes, UK. [6]Jet Propulsion Laboratory, California Institute of Technology, Pasadena, CA, USA. [7]Department of Astronomy and Carl Sagan Institute, Cornell University, Ithaca, NY, USA. [8]National Institute of Science Education and Research (NISER), HBNI, Jatni, Odisha, India. [9]Department of Physics, and Institute for Research on Exoplanets, Université de Montréal, Montreal, Canada. [10]Department of Physics (Atmospheric, Oceanic and Planetary Physics), University of Oxford, Oxford, UK. [11]Astrophysics Group, School of Physics and Astronomy, University of Exeter, Exeter, UK. [12]Department of Astrophysical Sciences, Princeton University, Princeton, NJ, USA. [13]School of Physics, University of Bristol, Bristol, UK. [14]Lunar and Planetary Laboratory, Department of Planetary Sciences, Univ. of Arizona, Tucson, AZ, USA. [15]Division of Geological and Planetary Sciences, California Institute of Technology, Pasadena, CA, USA.

* e-mail: tmevans@mpia.de

The temperature profile of a planetary atmosphere is a key diagnostic of radiative and dynamical processes governing the absorption, redistribution, and emission of energy. Observations have revealed dayside stratospheres that either cool[1,2] or warm[3,4] with altitude for a small number of gas giant exoplanets, while others are consistent with constant temperatures.[5-8] Here we report spectroscopic phase curve measurements for the gas giant WASP-121b,[9] which constrain stratospheric temperatures throughout the diurnal cycle. Variations measured for a water vapour spectral feature reveal a temperature profile that transitions from warming with altitude on the dayside hemisphere to cooling with altitude on the nightside hemisphere. The data are well explained by models assuming chemical equilibrium, with water molecules thermally dissociating at low pressures on the dayside and recombining on the nightside.[10,11] Nightside temperatures are low enough for perovskite ($CaTiO_3$) to condense, which could deplete titanium from the gas phase[12,13] and explain recent non-detections at the day-night terminator.[14-17] Nightside temperatures are also low enough for refractory species, such as magnesium, iron, and vanadium, to condense. Detections[16-19] of these metals at the day-night terminator suggest, however, that if they do form nightside clouds, cold trapping does not efficiently remove them from the upper atmosphere.

WASP-121b is an ultrahot (>2,000 Kelvin) gas giant exoplanet orbiting an F6V star every 30.6 hours.[9] Previous observations have shown that the dayside hemisphere of WASP-121b has a thermal inversion, with a temperature profile that increases with increasing altitude or, equivalently, with decreasing atmospheric pressure.[3,20,21] The thermal inversion is thought to be caused by the presence of optical absorbers capturing a significant fraction of incident stellar radiation at low pressures in the atmosphere.[22-24] Observations of the planet during transit

geometry have identified a number of such absorbers, including gaseous Fe, Mg, Cr, V, and VO.[16-19]

Two full-orbit phase curves of WASP-121b were observed at epochs in 2018 and 2019 with the Hubble Space Telescope (HST) Wide Field Camera 3 (WFC3) infrared spectrograph. For each observation, a time series of spectra was acquired using the G141 grism, which covers the 1.12-1.64μm wavelength range. Further technical details of the observations are provided in Methods. A broadband light curve was produced by summing each spectrum in the time series across the full wavelength range (Extended Data Fig. 1). This light curve was fit by simultaneously modelling the planet signal and instrumental systematics, as described in Methods. Quantitative results are reported in Extended Data Table 1 and the best-fit model is shown in Fig. 1a, with orbital phases of 0 and 0.5 corresponding to the primary transit and secondary eclipse mid-times, respectively. As described in Methods, the best-fit phase curve model was inverted to generate a global temperature map for WASP-121b (Fig. 1b). On the dayside hemisphere temperatures exceed 3,000 Kelvin and drop to below 1,500 Kelvin in the coolest regions of the nightside hemisphere.

To recover the planetary emission spectrum at different orbital phases, light curves were generated for twelve spectroscopic channels across the 1.12-1.64μm wavelength range (Extended Data Fig. 2). These light curves were analysed using a similar method to the broadband light curve fit (see Methods). The measured emission maxima of the spectroscopic phase curves give the spectrum of the planetary dayside hemisphere, shown in Fig. 2a. In addition, phase-resolved emission spectra were generated by averaging the planetary flux inferred from the spectroscopic light curve fits across sixteen bins in orbital phase. The planetary emission spectrum recovered immediately prior to the primary transit is shown in Fig. 2b and is comprised almost entirely of

emission from the nightside hemisphere of the planet. At intermediate phases, the emission received from WASP-121b emanates from a combination of the dayside and nightside hemispheres.[25-28]

Wavelengths covered by the data are sensitive to an opacity band of H_2O vapour and continuum opacity of H^- (Fig. 2). The measured shape and amplitude of these spectral features allow the chemical abundances and vertical temperature profile of the atmosphere to be inferred.[1-4] To recover these properties from the data, a retrieval analysis was first performed on the dayside emission spectrum. As described in Methods, the overall heavy element enrichment ('metallicity') of the atmosphere was allowed to vary, with the relative abundances of individual elements held fixed to solar ratios, and a one-dimensional analytic temperature profile was adopted with three free parameters. As the metallicity and temperature profile were varied in the fitting, chemical abundances were computed assuming chemical equilibrium. Results of this analysis are reported in Extended Data Table 2, including a measured metallicity of $[\mathrm{M/H}] = 0.76^{+0.30}_{-0.62}$ (approximately 1-10x solar). A second retrieval analysis was also performed for the nightside emission spectrum. Due to the lower signal-to-noise, the atmospheric metallicity was held fixed to the value determined from the dayside retrieval analysis, leaving only the three temperature profile parameters free. As described in Methods, the contribution to the overall emission from the narrow crescent of dayside hemisphere visible at this phase was also factored in to the modelled emission.

The inferred dayside and nightside emission spectra are shown in Fig. 2 and the corresponding pressure-dependent temperatures, H_2O abundances, H^- abundances, and contribution functions are shown in Fig. 3. A dayside thermal inversion is inferred at the pressures probed by the data (below ~30 millibar), consistent with previous results.[3,20,21] On the dayside, the H_2O abundance drops sharply with decreasing pressure, due to thermal dissociation of

molecules.[10,11] Thermal ionisation also raises the abundance of free electrons, which bind with atomic hydrogen to form H^- (refs 7-11, 29). As temperatures decrease on the nightside, H_2O molecules recombine at low pressures. Rotational-vibrational transitions of H_2O molecules at near-infrared wavelengths increase the efficiency of radiative cooling in the upper atmosphere (Extended Data Fig. 3), resulting in temperature profiles that cool with decreasing pressure on the nightside (Fig. 3a). As described in Methods, consistent results for the dayside and nightside hemisphere properties were obtained when retrievals were performed at intermediate phases (Extended Data Figs 4-7) and when the assumption of chemical equilibrium was relaxed (Figs 2 and 3, Extended Data Fig. 8).

These measurements provide empirical constraints for the theory that refractory species may be lost from the upper atmosphere of highly-irradiated planets due to cold trap processes.[12] For example, due to the high temperature contrasts expected between the dayside and nightside hemispheres, refractory species could condense on the nightside and settle to deeper layers of the atmosphere, despite dayside temperatures being high enough to maintain them in the gas phase. However, day-night cold trapping of this kind might be avoided if vertical mixing is vigorous within the atmosphere, allowing condensates to be suspended aloft long enough for lateral winds to return them to the dayside hemisphere.[30, 31] Alternatively, condensates may gravitationally settle to deeper layers of the atmosphere and subsequently re-enter the gas phase as they are returned to lower pressures by updrafts.[13]

Condensation curves for relevant refractory species[31-33] are shown in Fig. 3a, namely, corundum (Al_2O_3), perovskite ($CaTiO_3$), VO, Fe, forsterite (Mg_2SiO_4), and enstatite ($MgSiO_3$). The corundum, perovskite, and Fe condensation curves are crossed during the WASP-121b diurnal cycle (Fig. 3a) and it is also likely that those of forsterite, VO, and enstatite are crossed in the

coolest regions of the nightside hemisphere (Fig. 1b). It is particularly significant that temperatures drop low enough for Fe, Ca, Mg, and V to condense, as recent observations have revealed these heavy metals in the gas phase at the day-night terminator.[16-19] Vertical mixing must therefore be operating efficiently within the atmosphere of WASP-121b, to avoid day-night cold trapping. This also appears to be the case for another ultrahot gas giant, WASP-76b, for which gaseous Fe has been detected at the eastern terminator but not detected at the cooler western terminator, where it has presumably condensed.[34] However, non-detections of Ti and TiO at the day-night terminator of WASP-121b complicate this picture,[14-17] as these gases should also form condensates such as perovskite and TiO_2 on the nightside. [31-33] It would be surprising if Ti-bearing condensates are efficiently cold trapped while other refractory species avoid a similar fate. This is especially true for V, which is chemically similar to Ti but an order of magnitude less abundant in the solar neighbourhood.[35,36] For now, this remains an outstanding puzzle, with a solution that may depend on additional factors such as variations in surface energies between different condensate species.[37]

The dayside and nightside emission spectra predicted by a cloud-free three-dimensional general circulation model (GCM) simulation generated for this study (Methods) and results from two published GCMs[10] are shown in Fig. 2. Good agreement with the data is obtained, suggesting that the GCMs have successfully captured much of the interplay between the radiation, chemistry, and dynamics of the WASP-121b atmosphere. The broadband phase curve predicted by the GCM simulation run for this study is also shown in Fig. 1, having an overall amplitude in respectable agreement with the data. However, around the quadrature phases (i.e. 0.25 and 0.75), the GCM underpredicts the planetary emission (see also Extended Data Figs 2 and 4). Nightside clouds are unlikely to explain this discrepancy, as they would be expected to lower the emission by blocking radiation from deeper, warmer layers of the atmosphere. Refractory clouds forming close to the

terminator region, however, could potentially boost the emission received from the dayside crescent by reflecting light from the host star.[21,38] Another possible explanation may be provided by the optically thick exosphere of WASP-121b that has been observed to extend to the planet's Roche limit,[18] well below the pressure range considered by the GCMs. Heated layers of the stellar-facing exosphere would be maximally visible at quadrature, raising the overall emission received from the planet, whereas at superior and inferior conjunction, the data are sensitive to deeper atmospheric layers due to the zenith viewing geometry (Fig. 3d), and as such are well matched by the GCM predictions (Fig. 2). Furthermore, the GCMs did not include opacities for gaseous metals such as Fe and Mg, which are known to be present in the atmosphere of WASP-121b[16-19] and could contribute significantly to the outgoing emission.[11] These effects, along with others not considered here, such as latent heat release from the dissociation/recombination of hydrogen[29] and atmospheric drag,[8,39] should be investigated in future modelling.

The dynamics and chemistry of ultrahot gas giants such as WASP-121b are exotic by solar system standards, driven by dramatic contrasts in the irradiation environments of the dayside and nightside hemispheres. Until now, it has proven challenging to explore these diurnal variations due to the narrow infrared wavelength coverage of HST.[8,40] For WASP-121b, these wavelengths are fortuitously sensitive to a pressure range that allows the transition from inverted to non-inverted temperature profiles to be mapped globally. Further insights are anticipated with the *James Webb Space Telescope*, which will enable higher signal-to-noise spectroscopy across the broader 0.8-11μm wavelength range. This will provide fuller coverage of the H^- opacity continuum and access to stronger H_2O bands at longer wavelengths, breaking the degeneracy between the two species. Additional spectral features, such as the CO spectral band at 4.5μm, will provide further leverage for constraining the chemical composition, thermal structure, and wind patterns of the atmosphere.

References

1. Stevenson, K. B. et al. Thermal structure of an exoplanet atmosphere from phase-resolved emission spectroscopy. *Science*. 346, 838 (2014).
2. Line, M. R. et al. No Thermal Inversion and a Solar Water Abundance for the Hot Jupiter HD 209458b from HST/WFC3 Spectroscopy. *Astron. J*. 152, 203 (2016).
3. Mikal-Evans, T. et al. Confirmation of water emission in the dayside spectrum of the ultrahot Jupiter WASP-121b. *Mon. Not. R. Astron. Soc*. 496, 1638 (2020).
4. Nugroho, S. K. et al. High-resolution Spectroscopic Detection of TiO and a Stratosphere in the Day-side of WASP-33b. *Astron. J*. 154, 221 (2017).
5. Nikolov, N. et al. Hubble PanCET: an isothermal day-side atmosphere for the bloated gas-giant HAT-P-32Ab. *Mon. Not. R. Astron. Soc*. 474, 1705 (2018).
6. Mansfield, M. et al. An HST/WFC3 Thermal Emission Spectrum of the Hot Jupiter HAT-P-7b. *Astron. J*. 156, 10 (2018).
7. Arcangeli, J. et al. H- Opacity and Water Dissociation in the Dayside Atmosphere of the Very Hot Gas Giant WASP-18b. *Astrophys. J*. 855, L30 (2018).
8. Kreidberg, L. et al. Global Climate and Atmospheric Composition of the Ultra-hot Jupiter WASP-103b from HST and Spitzer Phase Curve Observations. *Astron. J*. 156, 17 (2018).
9. Delrez, L. et al. WASP-121 b: a hot Jupiter close to tidal disruption transiting an active F star. *Mon. Not. R. Astron. Soc*. 458, 4025 (2016).
10. Parmentier, V., Fortney, J. J., Showman, A. P., Morley, C., Marley, M. S. From thermal dissociation to condensation in the atmospheres of ultra hot Jupiters: WASP-121b in context. *Astron. Astrophys*. 617, A110 (2018).
11. Lothringer, J. D., Barman, T., Koskinen, T. Extremely Irradiated Hot Jupiters: Non-oxide Inversions, H- Opacity, and Thermal Dissociation of Molecules. *Astrophys. J*. 866, 27 (2018).
12. Spiegel, D. S., Silverio, K., Burrows, A. Can TiO Explain Thermal Inversions in the Upper Atmospheres of Irradiated Giant Planets? *Astrophys. J*. 699, 1487 (2009).
13. Parmentier, V., Showman, A. P., Lian, Y. 3D mixing in hot Jupiters atmospheres. I. Application to the day/night cold trap in HD 209458b. *Astron. Astrophys*. 558, A91 (2013).

14. Evans, T. M. et al. An Optical Transmission Spectrum for the Ultra-hot Jupiter WASP-121b Measured with the Hubble Space Telescope. *Astron. J*. 156, 283 (2018).
15. Merritt, S. R. et al. Non-detection of TiO and VO in the atmosphere of WASP-121b using high-resolution spectroscopy. *Astron. Astrophys*. 636, A117 (2020).
16. Ben-Yami, M. et al. Neutral Cr and V in the Atmosphere of Ultra-hot Jupiter WASP-121 b. *Astrophys. J*. 897, L5 (2020).
17. Hoeijmakers, H. J. et al. Hot Exoplanet Atmospheres Resolved with Transit Spectroscopy (HEARTS). IV. A spectral inventory of atoms and molecules in the high-resolution transmission spectrum of WASP-121 b. *Astron. Astrophys*. 641, A123 (2020).
18. Sing, D. K. et al. The Hubble Space Telescope PanCET Program: Exospheric Mg II and Fe II in the Near-ultraviolet Transmission Spectrum of WASP-121b Using Jitter Decorrelation. *Astron. J*. 158, 91 (2019).
19. Gibson, N. P. et al. Revisiting the potassium feature of WASP-31b at high resolution. *Mon. Not. R. Astron. Soc*. 482, 606 (2019).
20. Bourrier, V. et al. Optical phase curve of the ultra-hot Jupiter WASP-121b. *Astron. Astrophys*. 637, A36 (2020).
21. Daylan, T. et al. TESS observations of the WASP-121 b phase curve. *Astron. J*. 161, 131 (2020).
22. Hubeny, I., Burrows, A., Sudarsky, D. A Possible Bifurcation in Atmospheres of Strongly Irradiated Stars and Planets. *Astrophys. J*. 594, 1011 (2003).
23. Burrows, A., Hubeny, I., Budaj, J., Knutson, H. A., Charbonneau, D. Theoretical Spectral Models of the Planet HD 209458b with a Thermal Inversion and Water Emission Bands. *Astrophys. J*. 668, L171 (2007).
24. Fortney, J. J., Lodders, K., Marley, M. S., Freedman, R. S. A Unified Theory for the Atmospheres of the Hot and Very Hot Jupiters: Two Classes of Irradiated Atmospheres. *Astrophys. J*. 678, 1419 (2008).
25. Feng, Y. K., Line, M. R., Fortney, J. J. 2D retrieval frameworks for hot Jupiter phase curves. *Astron. J.* 169, 137 (2020).
26. Taylor, J. et al. Understanding and mitigating biases when studying inhomogeneous emission spectra with *JWST*. *Mon. Not. R. Astron. Soc*. 493, 4342 (2020).
27. Irwin, P. G. J. et al. 2.5 retrieval of atmospheric properties from exoplanet phase curves: application to WASP-43b observations. *Mon. Not. R. Astron. Soc*. 493, 106 (2020).

28. Changeat, Q., Al-Refaie, A. TauREx3 PhaseCurve: a 1.5D model for phase-curve description. *Astrophys. J.* 898, 155 (2020).

29. Bell, T. J., Cowan, N. B. Increased Heat Transport in Ultra-hot Jupiter Atmospheres through H- Dissociation and Recombination. *Astrophys. J*. 857, L20 (2018).

30. Heng, K., Demory, B-.O. Understanding Trends Associated with Clouds in Irradiated Exoplanets. *Astrophys. J*. 777, 100 (2013).

31. Helling, C. et al. Understanding the atmospheric properties and chemical composition of the ultra-hot Jupiter HAT-P-7b. I. Cloud and chemistry mapping. *Astron. Astrophys*. 631, A79 (2019).

32. Burrows, A., Sharp, C. M. Chemical Equilibrium Abundances in Brown Dwarf and Extrasolar Giant Planet Atmospheres. *Astrophys. J*. 512, 843 (1999).

33. Wakeford, H. R. et al. High-temperature condensate clouds in super-hot Jupiter atmospheres. *Mon. Not. R. Astron. Soc*. 464, 4247 (2017).

34. Ehrenreich, D. et al. Nightside condensation of iron in an ultrahot giant exoplanet. *Nature*. 580, 597 (2020).

35. Lodders, K. Titanium and Vanadium Chemistry in Low-Mass Dwarf Stars. *Astrophys. J*. 577, 974 (2002).

36. Asplund, M., Grevesse, N., Sauval, A. J., Scott, P. The Chemical Composition of the Sun. Annual Review of *Astron. Astrophys*. 47, 481 (2009).

37. Gao, P. et al. Aerosol composition of hot giant exoplanets dominated by silicates and hydrocarbon hazes. *Nature Astronomy*. 4, 951 (2020).

38. Parmentier, V. et al. Transitions in the cloud compositions of hot Jupiters. *Astrophys. J*. 828, 22 (2016).

39. Komacek, T. D., Showman, A. P., Tan, X. Atmospheric circulation of hot Jupiters: dayside-nightside temperature differences. II. Comparison with observations. *Astrophys. J*. 835, 198 (2017).

40. Arcangeli, J. et al. Climate of an ultra hot Jupiter. Spectroscopic phase curve of WASP-18b with HST/WFC3. *Astron. Astrophys*. 625, A136 (2019).

Figures

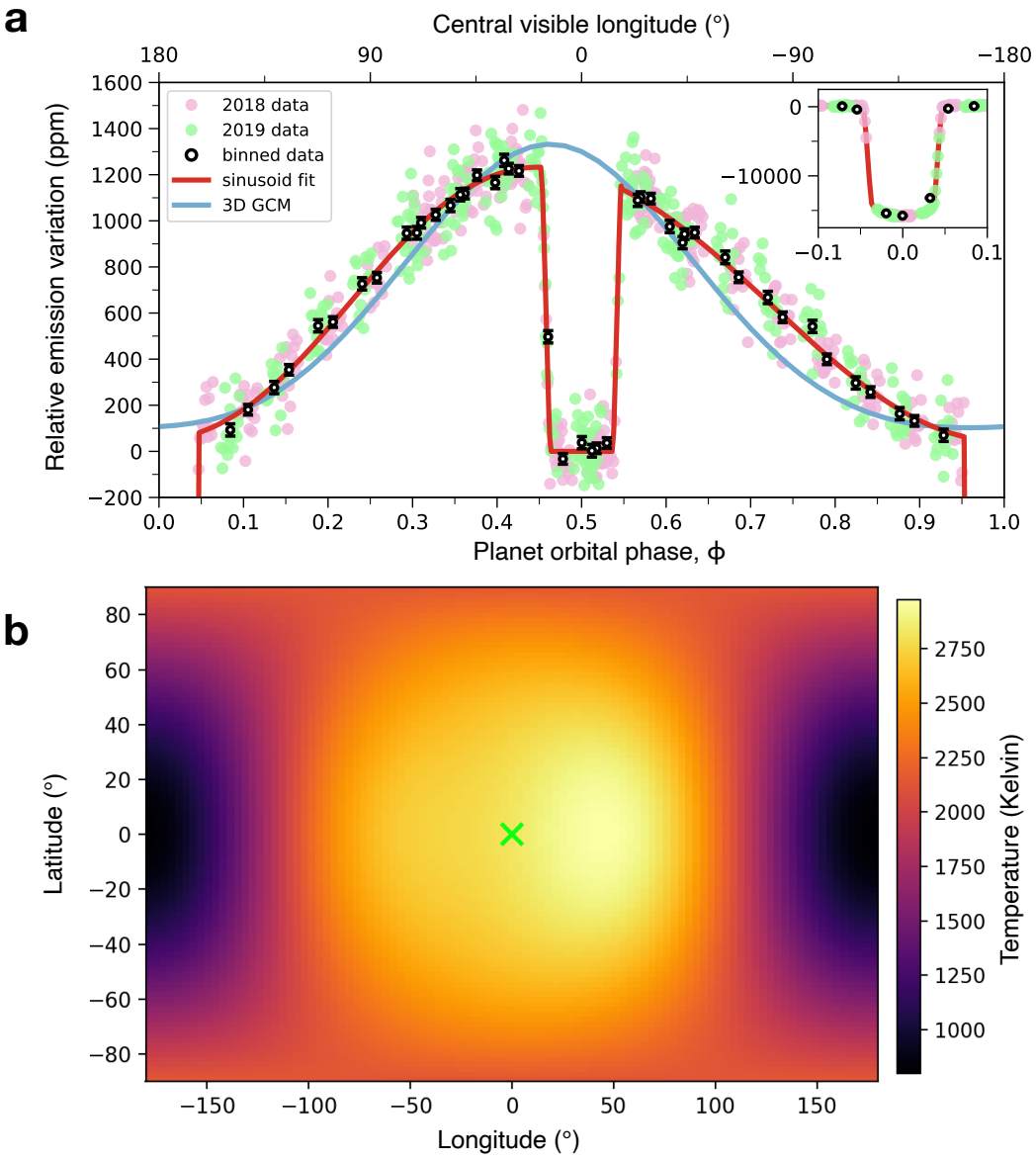

Fig. 1. Broadband phase curve and inverted temperature map for WASP-121b. a, Planet emission relative to the host star emission as a function of the planetary orbital phase. Pink and green circles show WFC3 measurements made at epochs in 2018 and 2019, respectively. Black circles show binned data for individual HST orbits, with error bars indicating the 1σ measurement uncertainties. Red line shows the maximum likelihood second-order sinusoidal model, including primary transit and secondary eclipse signals. Blue line shows the prediction of a 3D GCM simulation. Inset shows the full primary transit signal. **b,** Latitude-longitude temperature map obtained by inverting the maximum likelihood phase curve model as described in Methods. Green cross indicates the location of the substellar point.

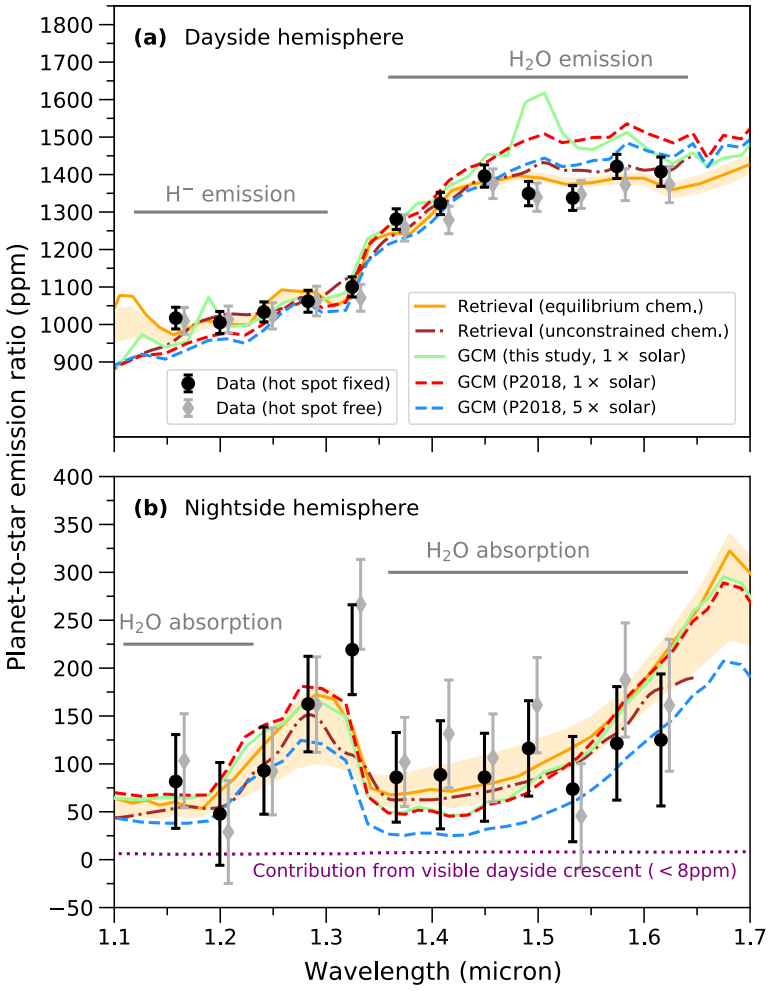

Fig. 2. Emission spectra for the dayside and nightside hemispheres of WASP-121b. a, Black circles show measured dayside emission with error bars corresponding to 1σ measurement uncertainties. Grey diamonds show the same, but for a light curve analysis in which the phase of maximum brightness ('hot spot') was allowed to vary in each spectroscopic channel (see Methods) and with small horizontal offsets applied for visual clarity. Orange solid line shows the maximum likelihood model and yellow shading shows the 1σ credible range of model predictions from the ATMO retrieval analysis assuming chemical equilibrium. Brown dot-dashed line shows the maximum likelihood model from the NEMESIS retrieval analysis with unconstrained chemistry (see Methods). Light green solid line shows the prediction of the 3D GCM run for this study. Dashed red and blue lines show predictions of the 3D GCMs for WASP-121b published in ref. 13 assuming metallicities of 1x and 5x solar, respectively. **b,** The same as **a**, but showing results for the nightside hemisphere emission obtained at orbital phase 0.95, immediately prior to primary transit ingress. Dotted purple line also shows the emission contribution from the narrow crescent of dayside hemisphere visible at this orbital phase, which does not exceed 8ppm across the wavelengths covered by the data.

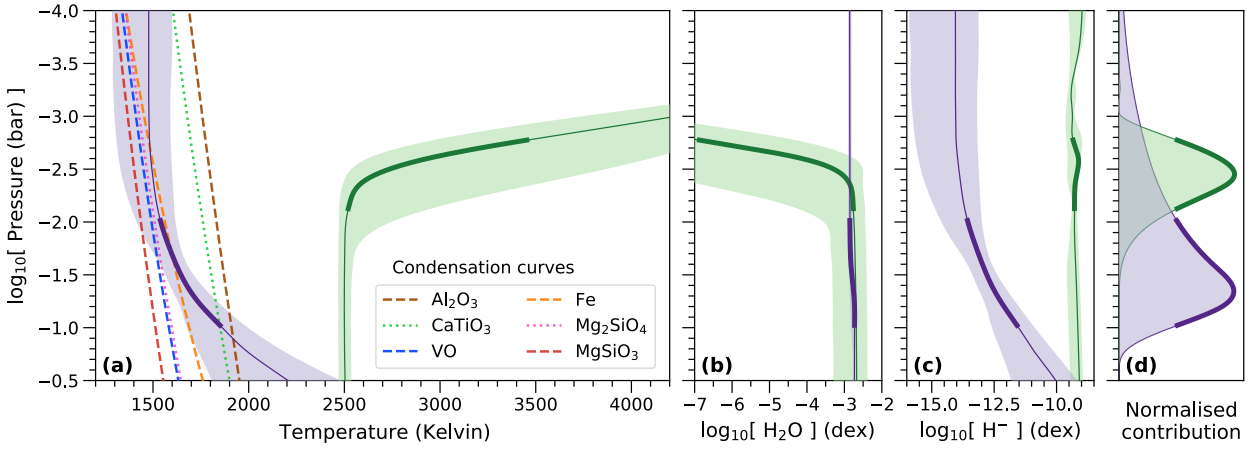

Fig. 3. Pressure-dependent atmospheric properties retrieved for WASP-121b. a, Green solid line shows the median temperature at each pressure level inferred for the dayside hemisphere by the ATMO retrieval analysis, with green shading showing the 1σ credible range. Purple solid line and purple shading show the same, but for the nightside hemisphere. Thick sections of the purple and green lines indicate the pressure levels from which the majority of the planetary emission is emanating at the wavelengths covered by the data. **b, c,** Vertical abundances for H_2O and H^-, using the same colour scheme as panel **a**. The narrow range of allowed H_2O abundances for the nightside is a result of the fixed metallicity. For H^-, the nightside abundance is more uncertain than for the dayside, because no H^- spectral features are detected in the nightside spectrum. However, the H^- abundance can still vary under the assumption of chemical equilibrium within the range of allowed temperatures, as the latter mediates the abundance of free electrons through thermal ionisation. **d,** Normalised contribution functions for the dayside and nightside hemispheres, integrated across the wavelength range covered by the data, using the same colour scheme as panel **a**.

METHODS

Observations and data reduction

Two full orbit phase curves of WASP-121b were observed on 2018 March 12-13 and 2019 February 3-4 using the Hubble Space Telescope (HST) Wide Field Camera 3 (WFC3) infrared spectrograph with the G141 grism, covering a wavelength range of approximately 1.12-1.64μm micron. Each observation was performed over 26 consecutive HST orbits and lasted approximately 40.3 hr. The timing of each observation was designed to encompass two consecutive secondary eclipses, as these correspond to times when only the star is visible, allowing the baseline flux level to be calibrated at the beginning and end of the observation. Furthermore, both observations were scheduled such that the combined dataset provided maximum phase coverage for the planetary orbit, which has a period of 30.6 hr. Due to the long duration of the observations, full guide star reacquisition sequences were performed at the beginning of the 10th and 20th HST orbits. Integration times per exposure were 103 sec over 15 non-destructive reads (NSAMP=15) using the SPARS10 sampling sequence. Science exposures were made using the spatial scanning mode with scans along approximately 60 pixel rows of the detector cross-dispersion axis at a rate of 0.073 arcsec sec^{-1}. With this setup, 415 exposures were acquired for each phase curve observation. Peak frame counts were kept below ~40,000 electrons $pixel^{-1}$, within the recommended range for the detector.[41]

Spectra were extracted from each data frame using a custom Python code.[3,42-44] In brief, this involved first estimating the background flux for each exposure by taking the median count within a 10×170 pixel box away from the target on the detector. The background was then subtracted from each exposure and the target flux summed along the cross-dispersion axis within

a rectangular aperture spanning 100 pixel rows, giving the target flux as a function of location along the detector dispersion axis. The mapping from the dispersion axis to wavelength was determined by cross-correlating these measured fluxes against a model stellar spectrum modulated by the G141 grism throughput.

Broadband light curve analysis

Broadband light curves were produced by integrating the time series of target spectra across the dispersion axis and are shown in Extended Data Fig. 1. The primary transits, secondary eclipses, and phase curve variations for the planet are easily visible by eye. However, the data are also affected by instrumental systematics caused by charge-trapping on the detector, producing a ramp-like trend in each HST orbit. In addition, longer-term instrumental drifts are evident, particularly at the beginning of the observations, and subtle discontinuities affect the measured flux at the HST orbits immediately following guide star reacquisitions.

We modelled both light curves jointly to extract properties of the planet. Our overall model M took the form:

$$M_{kj} = B_{kj} \cdot \Psi_k \cdot \Pi \qquad (1)$$

where B is the instrumental baseline trend, Ψ is the detector ramp systematic, and Π is the astrophysical signal. Here, the 'k' subscripts refer to the observation number (k=1 for the 2018 observation and k=2 for the 2019 observation) and the 'j' subscripts refer to the data segment number. For the latter, we divided each observation into three data segments, defined by the guide star re-acquisitions (Extended Data Fig. 1). In summary, we modelled: three data segments with independent baseline trends, for each observation; ramp systematics separately for each

observation but shared across data segments; and a planet signal shared across all data segments of both observations.

For B_{kj}, we followed standard practice[8,40] and adopted a quadratic trend in time t for the first data segment (j=1) of each visit. For the second (j=2) and third (j=3) data segments, we adopted linear t trends. This was done because the baseline drift is clearly less pronounced following the first data segment (Extended Data Fig. 1), as the spacecraft and instrument has settled into a stable configuration. We also tested quadratic t trends for j=2 and j=3, but found this did not improve the quality of the fit, justifying the use of the simpler linear t trends.

For Ψ_k, we adopted the analytic treatment of ref. 45, which is motivated by a simple model of electron charge-trapping on the detector. Explicitly:

$$\Psi(t,\tau) = r \cdot \rho \ , \tag{2}$$

where τ is the time from the start of each HST orbit, and:

$$r = 1 + a_1 \cdot \exp[\ -t/a_2\ ] \ , \tag{3}$$

$$\rho = 1 + a_3 \cdot \exp[\ -(\ t - \tau\ )/(\ a_4 \cdot r\ )\ ] \ . \tag{4}$$

The astrophysical signal Π is comprised of the combined flux received from the star-planet system:

$$\Pi = F_s + F_p \ , \tag{5}$$

where F_s is the emission from the host star and F_p is the emission from the planet. The stellar flux F_s is assumed to be constant except when the planet transits in front of the host star. We used a publicly available software package[46] to compute the drop in $F_s(t)$ during primary transit. We modelled the planet emission signal as:

$$F_p = [\ \Phi + \Gamma\ ] \cdot E \ , \tag{6}$$

where Φ denotes the phase variations, Γ is the drop in flux received from the planet during secondary eclipse, and E are ellipsoidal variations caused by tidal distortion of the planet. For Φ, we used a second-order cosine function:

$$\Phi = c_0 + (c_1/2)\cdot [\ 1 - \cos(\ \phi - c_2\ )\ ] + (c_3/2)\cdot[\ 1 - \cos(\ 2\phi - c_4\ )\ ]\ , \qquad (7)$$

where $\phi=2\pi\cdot(t - T_p)/P$ is the planetary orbital phase and T_p is the time of mid-transit. To compute Γ, we used the same publicly available software used for the primary transit signal.[46] For E, we used a cosine function of the form:

$$E = 1 + (\varepsilon_0/2)\cdot[\ 1 - \cos(\ 2\phi\ )\ ]\ , \qquad (8)$$

giving maximum cross-sectional area at orbital quadrature.

Using the above model, we defined a log-likelihood function for the joint dataset of the form:

$$\log P = \log N(\ \boldsymbol{y}_1 - \boldsymbol{M}_1, K_1\ ) + \log N(\ \boldsymbol{y}_2 - \boldsymbol{M}_2, K_2\ ) \qquad (9)$$

where $N(\ \boldsymbol{\mu}, K\ )$ denotes a multivariate normal distribution with mean vector $\boldsymbol{\mu}$ and covariance matrix K. In Eq. 9, the mean vector is given by the t-dependent model residuals, where $\boldsymbol{y}_k$ is a vector containing the data points and $\boldsymbol{M}_k$ is a vector containing the corresponding model values for the kth observation. The covariance matrices for each observation are assumed to be diagonal, with the form $K_{kk}=\beta_k\sigma_k I$, where σ_k is the photon noise value, β_k is a white noise rescaling factor, and I is the identity matrix.

For the systematics components, our free parameters were the coefficients for the t-dependent baseline trends (B_k); the $a_{1,k}$, $a_{2,k}$, $a_{3,k}$, and $a_{4,k}$ parameters for the detector ramps (Ψ_k); and the white noise rescaling factors β_k. For the primary transit (i.e. F_s), the following parameters were allowed to vary: planet-to-star radius ratio ($R_p/R_\star$); normalised semimajor axis ($a/R_\star$); orbital impact parameter ($b=a\cdot\cos i/R_\star$, where i is the orbital inclination); and the primary transit mid-

227 times (T_p). These parameters were shared across both datasets, except for T_p which was allowed to
228 vary separately for each dataset. Since the planetary orbital period has been previously determined
229 to a high level of precision, it was fixed to P=1.2749247646 day.[18] A circular orbit was assumed,
230 given constraints from previous measurements.[9] A quadratic stellar limb darkening profile was
231 adopted with coefficients (u_1, u_2) fixed to values determined using a model of the host star
232 atmosphere, as described previously. For the phase variations Φ, the parameters c_0, c_1, c_2, c_3, and
233 c_4 were allowed to vary. For Γ, the secondary eclipse mid-time T_s was linked to the primary transit
234 mid-time T_p according to T_s=T_p+P/2, given the assumed circular orbit. Rather than treating the
235 eclipse depth as a separate free parameter, it was constrained such that F_p=0 at the bottom of
236 eclipse. The ellipsoidal variation in the planetary cross-sectional area, ε_0, was also treated as a free
237 parameter. Uniform priors were adopted for all free parameters. Marginalisation of the posterior
238 distribution was performed using affine-invariant Markov chain Monte Carlo (MCMC) with 300
239 walkers and 1,600 steps, as implemented by a publicly available software package.[47] The best-fit
240 model is shown in Fig. 1a and the results for the astrophysical model parameters are summarised
241 in Extended Data Table 1.

242 In addition, a simpler first-order sinusoidal model was tested, equivalent to fixing c_3 = c_4
243 = 0 in Eq. 7. The results of this fit are also reported in Extended Data Table 1, with good agreement
244 obtained for parameters common to both models. However, the first-order sinusoidal model has a
245 significantly higher Bayesian Information Criterion (BIC) value of 2129.5 compared to 2111.0 for
246 the second-order sinusoidal model, corresponding to a Bayes factor of $\exp(-\Delta\mathrm{BIC}/2)=10^4$ in
247 favour of the second-order sinusoidal model. This provides strong evidence for asymmetry in the
248 phase curve about the 'hot spot' (i.e. phase of peak emission), which is better accounted for by the

second-order sinusoidal model than by the first-order sinusoidal model. For this reason, the second-order sinusoidal model is adopted as the preferred fit for the broadband light curve.

Extended Data Table 1 reports the heat redistribution factors A_F obtained for the first-order and second-order sinusoidal model fits. These were derived by computing $A_F=(F_{max}-F_{min})/F_{max}$ for each phase curve model sampled, where F_{max} and F_{min} are the maximum and minimum values of the phase curve. The obtained value for A_F (95.1±2.5% for the preferred second-order sinusoid and 98.6±1.9% for the first-order sinusoid) is broadly in line with those reported for the three other gas giant exoplanets with published WFC3 phase curve measurements: A_F=100.5±1.3% for WASP-43b,[1,48] A_F=91±2% for WASP-103b,[8] and A_F>96% for WASP-18b.[40]

A spherical harmonic of degree l=2 was also used to generate a temperature map of the planet. The temperature map was converted to a corresponding phase curve signal in the G141 passband using a publicly available code.[49] Coefficients were adjusted to optimise the match of the resulting phase curve with the second-order sinusoidal function derived from the light curve fits (Extended Data Fig. 9). Since the available phase curve data do not constrain latitudinal temperature variations, coefficients of order m=0 were fixed to zero. The resulting temperature map is shown in Fig. 1b. At longitudes approximately 9° eastward of the substellar point, the atmosphere reaches its highest temperatures of around 3,200 Kelvin. On the nightside hemisphere, the coldest regions of the atmosphere are around 1,200 Kelvin, cool enough for numerous refractory species to condense (Fig. 3a).

Spectroscopic light curve analysis

Spectroscopic light curves were generated by binning the spectra into twelve wavelength channels. Before doing this, systematics common to all wavelengths were corrected using a cross-correlation

technique[3,42-44] based on an original implementation by ref. 48. This common-mode correction effectively cleaned the detector ramp systematics in all but the first HST orbit of both datasets. It also significantly reduced the baseline trend systematics due to instrumental drift.

Since the common-mode correction successfully removed most of the systematics affecting each spectroscopic channel, a simpler model than described above for the broadband analysis was adopted for the light curve fitting. Rather than fit a quadratic time trend for the instrumental baseline of the first data segments (i.e. the B_{k1} terms of Eq. 1), linear time trends were used for all data segments. Furthermore, with the exception of the first HST orbit of each dataset, a model for the detector ramp was unnecessary. We therefore opted to discard the first HST orbit from each spectroscopic light curve and effectively set Ψ_k=1 (Eq. 1) for the remaining orbits. The astrophysical signal was modelled using the same model Π as was used for the broadband light curve fit. However, for the spectroscopic light curve fits, a number of parameters were held fixed to the best-fit values determined from the broadband light curve (Extended Data Table 1), namely: T_p, a/R_s, and b, which do not vary with wavelength, and the ellipsoidal variation amplitude, ε_0. Quadratic limb darkening coefficients (u_1, u_2) were determined for each spectroscopic channel as for the broadband light curve, and also held fixed during fitting. Aside from these details, light curve fitting proceeded as for the broadband light curve. The results of these fits are reported in Extended Data Table 3 and the inferred wavelength-dependent hot spot phases are shown in Extended Data Fig. 10. A second suite of spectroscopic light curve fits was also performed with the hot spot phase (c_2) and higher-order phase curve terms (c_3, c_4) held fixed to the maximum likelihood values derived from the broadband light curve fit. The results of these fits are reported in Extended Data Table 4. Derived heat redistribution factors A_F (see above) for both suites of spectroscopic light curve fits are reported in Extended Data Table 5.

In all spectroscopic wavelength channels, the fits for which c_2, c_3, and c_4 were held fixed have lower BIC values than the fits for which these parameters were allowed to vary freely (Extended Data Table 5). For this reason, to derive the phase-resolved emission spectra of WASP-121b we adopt the light curve fits for which c_2, c_3, and c_4 were held fixed and show the corresponding best-fit light curves in Extended Data Fig. 2. To extract the phase-resolved emission spectra, the measured planetary emission for each spectroscopic light curve shown in Extended Data Fig. 2 was binned into sixteen orbital phase bins, centred at phases ϕ = 0.05, 0.12, 0.17, 0.23, 0.28, 0.32, 0.38, 0.43, 0.57, 0.62, 0.68, 0.72, 0.78, 0.82, 0.88, and 0.95, where ϕ = 0 coincides with the primary transit mid-point and ϕ = 0.5 coincides with the secondary eclipse mid-point. Each phase bin had an effective width of 1.5 hours with the exception of the bins centred at ϕ = 0.05 and ϕ = 0.95, which had larger widths of 3 hours to compensate for the lower fluxes at those phases. Uncertainties were calculated as the standard deviation of model residuals within each phase bin added in quadrature to the standard deviation of in-eclipse model residuals (i.e. the uncertainty in the stellar baseline flux level), following ref. 8. The planetary emission measurements obtained in this way are reported in Extended Data Table 6 and plotted in Extended Data Figure 4. As described in the main text, a dayside emission spectrum was also generated from the distribution of light curve emission maxima generated during the fitting. This dayside spectrum is reported in Extended Data Table 7 and, as shown in Extended Data Fig. 11, is in excellent agreement with the spectrum obtained from the emission measured in the phase bin immediately preceding secondary eclipse ingress. It also has a similar shape but a slightly higher overall level than the emission measured in the phase bin immediately following eclipse egress. Both of these observations are consistent with expectations, as the phase curve peak coincides with the phase bin immediately preceding eclipse ingress (Fig. 1 and Extended Data Table 1). Furthermore, the secondary eclipse

spectrum presented by ref. 3 also has a similar shape, but intermediate overall level, relative to these spectra (Extended Data Fig. 11). Again, this is to be expected, as the secondary eclipse depths of ref. 3 were measured relative to an out-of-eclipse baseline that was linear in *t* and thus effectively the average of the emission measured immediately before and after eclipse.

Retrieval analyses assuming chemical equilibrium

Atmospheric retrieval analyses were performed on the phase-resolved emission spectra using ATMO, a one-dimensional radiative transfer code used to simulate substellar atmospheres.[51-60] ATMO solves the radiative transfer equation in plane-parallel geometry assuming hydrostatic and radiative-convective equilibrium. The first step of the analysis was to perform a retrieval on the dayside spectrum derived from the measured emission maxima in each spectroscopic wavelength channel (Extended Data Table 7). For this retrieval, the pressure-temperature (PT) profile was freely fit using the analytic profile of ref. 61, with three free parameters: the infrared opacity (κ_{IR}); the ratio of the visible-to-infrared opacity ($\gamma=\kappa_V/\kappa_{IR}$); and an irradiation efficiency factor (ψ). The atmosphere was assumed to be in chemical equilibrium, with the heavy element abundances (i.e. metallicity) varied as a free parameter ([M/H]). Chemical abundances were calculated using Gibbs energy minimisation for 175 gaseous species, 9 ionic species, and 93 condensate species.[56-59] Rainout of condensed species consistent with the retrieved PT profiles was included,[57] as was thermal ionisation and dissociation. Opacities for the spectrally active species H_2O, CO_2, CO, CH_4, NH_3, Na, K, Li, Rb, Cs, TiO, VO, FeH, PH_3, H_2S, HCN, C_2H_2, SO_2, Fe, and H^- were included, along with collision-induced absorption due to H_2–H_2 and H_2–He. Uniform priors were adopted for all model parameters (κ_{IR}, γ, ψ, [M/H]) and fitting was performed using nested sampling.[62-64] An ATLAS model[65] was adopted for the stellar spectrum, assuming a stellar effective temperature

$T_\star$=6,500 Kelvin, surface gravity log $g_\star$=4.0 cm·s^{-2}, and radius $R_\star$=1.458 solar radii, based on the values provided by ref. 9. The resulting posterior distributions are reported in Extended Data Table 2 and the corresponding emission spectrum distribution is shown in Fig. 2a. The maximum likelihood model has a χ^2 value of 9.74 for 8 degrees of freedom (i.e. reduced $\chi^2_v = 1.2$), indicating a good fit to the data. Also shown in Fig. 3 are posterior distributions for the PT profile (Fig. 3a), H_2O abundance (Fig. 3b), and H^- abundance (Fig. 3c), and the contribution function for the maximum likelihood model (Fig. 3d). Note that the H_2O and H^- abundances were determined from the chemical equilibrium abundances and were not fit directly as free parameters.

For the remaining phase-resolved emission spectra, varying fractions of the dayside and nightside hemispheres are visible. Due to the strong contrast in effective temperature between each hemisphere, the dayside and nightside spectra are expected to differ significantly. To accommodate this, retrievals were performed using a method similar to the "2TP-Fixed" framework described by ref. 25. Under this approach, denoted here as "2x PT", the combined emission received from the planet Φ at each orbital phase was assumed to be described by:

$$\Phi = \eta_d \Phi_d + (1 - \eta_d)\Phi_n \quad (10)$$

where η_d is the fractional area of the visible dayside hemisphere, Φ_d is the planetary emission from the dayside hemisphere, and Φ_n is the planetary emission from the nightside hemisphere. The fractional area of the visible dayside hemisphere η_d is given by:

$$\eta_d = [\,1 - \cos(\,2\pi\phi + \pi - c_2\,)\,]/2 = [\,1 + \cos(\,2\pi\phi - c_2\,)\,]/2 \quad (11)$$

This is a slight variation of Equation A2 in ref. 25, with c_2 corresponding to the phase of maximum brightness and set to the value obtained from the broadband light curve fit (Extended Data Table 1). Given that the data are sensitive to thermal emission, rather than reflected light, the inclusion of the c_2 offset accounts for the overall advection of gas prior to re-emission. The dayside emission

Φ_d was also held fixed to the maximum likelihood model described above and shown in Fig. 2a. This was done because the dayside spectrum derived from the emission maxima has a relatively high signal-to-noise and retrieving for both the dayside and nightside contributions at each orbital phase was not justified given the limited number of data points (i.e. twelve spectroscopic channels). The metallicity was also assumed to be the same for both hemispheres and held fixed to [M/H]=0.7 (i.e. 5x solar), close to the median value derived from the dayside spectrum (Extended Data Table 2). With the metallicity and dayside emission held fixed, this left the three PT profile parameters (κ_{IR}, γ, ψ) for the nightside hemisphere as the remaining free parameters. As for the initial retrieval for the dayside spectrum described above, fitting was again performed using nested sampling, with uniform priors for the PT profile parameters. The nightside PT profiles were retrieved in this way for phases ϕ = 0.05, 0.12, 0.17, 0.23, 0.28, 0.72, 0.78, 0.82, 0.88, and 0.95. Useful constraints could not be obtained by fitting for the nightside PT profiles at the remaining phases (i.e. ϕ = 0.32, 0.38, 0.43, 0.57, 0.62, 0.68), as the nightside emission Φ_n comprised a relatively insignificant fraction of the total planetary emission. For these latter phases, Φ_n was instead held fixed to the maximum likelihood model obtained for the ϕ = 0.95 retrieval (Fig. 2b), as the nightside emission had the highest signal-to-noise at this phase, and the PT profile was instead allowed to vary for the dayside emission component Φ_d. Resulting phase-resolved emission spectra are shown for all phases in Extended Data Fig. 4. The corresponding PT profiles, H_2O abundances, and H^- abundances are shown in Extended Data Figs 5, 6, and 7, respectively. The χ^2 fit statistics are reported in Extended Data Table 8, with a mean reduced $\chi^2_\upsilon = 1.1$ and median reduced $\chi^2_\upsilon = 1.2$ achieved across the sixteen phase bins. One final retrieval was performed for phase ϕ = 0.95, the same as before (i.e. dayside contribution held fixed and PT parameters allowed to vary) but with the metallicity also allowed to vary as a free parameter. The

results of this retrieval are given in Extended Data Table 2 and the inferred metallicity ([M/H]=$0.66^{+0.70}_{-1.02}$) is found to be consistent with the [M/H]=0.7 (i.e. 5x solar) value assumed for the fiducial retrievals, providing a useful validation of the latter.

To assess the significance of the nightside emission detections, the χ^2 and BIC values were computed under the assumption of zero nightside emission (i.e. $\Phi_n = 0$) at the ten phases for which the "2x PT" retrievals were performed for the nightside hemisphere. As reported in Extended Data Table 9, the BIC values of the "2x PT" retrievals are lower than those of the retrievals assuming $\Phi_n = 0$ for seven of the ten phases considered. At three of the individual phases (ϕ = 0.23, 0.88, 0.95) the Bayes factors are >100, corresponding to decisive preference for the "2x PT" models over the $\Phi_n = 0$ null hypothesis.[66,67] The strongest preference for the "2x PT" retrieval is seen at phase ϕ = 0.95, for which the null hypothesis is disfavoured by a Bayes factor of 7.1×10^{10}. This translates to a preference for the "2x PT" model over the $\Phi_n = 0$ null hypothesis at a significance in excess of 5σ under the frequentist paradigm, following the conversion provided by ref. 68. If all ten phases are considered together as an ensemble, the BIC is 221.3 for the "2x PT" retrievals and 380.1 for the $\Phi_n = 0$ null hypothesis (last row of Extended Data Table 9), amounting to an overall rejection of the null hypothesis with a Bayes factor of 3×10^{34}. The unambiguous preference for the "2x PT" models over the $\Phi_n = 0$ null hypothesis at multiple phases implies that emission from the nightside hemisphere is distinct from the dayside contribution and detected at high confidence in the data.

As an additional check, simple blackbody spectra were fit to each phase-resolved emission spectrum. For these fits, the effective planetary temperature was the only free parameter. The maximum likelihood spectra are plotted in Extended Data Figure 4 and the results are reported in Extended Data Table 8. These blackbody fits had a mean reduced $\chi^2_\nu = 2.1$ and median reduced

$\chi_v^2 = 2.0$ across the sixteen phase bins, which is significantly poorer than those obtained for the "2x PT" fits (Extended Data Table 8). However, the brightness temperatures derived from the blackbody fits for the dayside and nightside hemispheres allow simple estimates to be made for the planetary Bond albedo (A_B) and heat redistribution efficiency (ε) following the method of ref. 69. The results of this analysis are shown in Extended Data Fig. 12a. As can be seen in Extended Data Fig. 12b, the Bond albedo derived for WASP-121b (A_B = 0.14 ± 0.08) is consistent with values reported for other hot Jupiters that have similar irradiation temperatures ($T_0 = T_\star\sqrt{R_\star/a} = 3320 \pm 72$ K for WASP-121b). However, the derived value for the heat redistribution efficiency (ε = 0.29 ± 0.02 for WASP-121b) is notably higher than for two of those shown in Extended Data Fig. 12c with similar irradiation temperatures: namely, WASP-18b ($T_0 = 3412 \pm 49$, $\varepsilon = 0.01^{+0.07}_{-0.01}$)[70] and KELT-1b ($T_0 = 3391 \pm 29$, $\varepsilon = 0.06^{+0.03}_{-0.02}$).[70] These measurements hint at a diversity of circulation regimes among highly-irradiated substellar objects.

Retrieval analyses with unconstrained chemistry

A second suite of retrieval analyses was performed using the NEMESIS radiative transfer and retrieval model.[26,27,71-74] NEMESIS couples a parametric, one-dimensional radiative transfer simulation to the PyMultiNest algorithm[75] which uses nested sampling to explore the model parameter space.[60-62] The correlated-k approximation[76] is used to pre-tabulate gas absorption data.

There were a number of important differences between the approaches used by ATMO and NEMESIS to model the WASP-121b atmosphere. First, the NEMESIS retrievals only fit for the abundances of H_2O and H^-; the two other main species expected to be spectrally significant at the wavelengths probed by the data are VO and FeH (Extended Data Fig. 3), which were included with a constant mole fraction fixed to the values inferred by ref. 20. Second, the abundances of

H_2O and H^- were allowed to vary freely at each orbital phase, without the requirement of satisfying chemical equilibrium. Third, following ref. 10, a simple analytic treatment was adopted to account for thermal dissociation of H_2O at phases for which the dayside was retrieved (i.e. ϕ = 0.32, 0.38, 0.43, 0.57, 0.62, 0.68). Specifically, the following parameterisation for the H_2O mole fraction (X) as a function of pressure (P) was adopted:

$$X(P) = \begin{cases} X_{\mathrm{deep}} & \text{for } P \geq P_{\mathrm{knee}} \\ X_{\mathrm{deep}}(P/P_{\mathrm{knee}})^{\alpha} & \text{for } P < P_{\mathrm{knee}} \end{cases} \quad (12)$$

where the deep atmosphere H_2O mole fraction (X_{deep}), knee pressure (P_{knee}), and power law index (α) were fitted as free parameters. As in ref. 20, H^- was assumed to be well-mixed throughout the atmosphere, with constant mole fraction retrieved as an additional parameter. The remaining atmosphere was assumed to be composed of H_2 and He in a 9:1 ratio.

The H_2O, VO, and FeH k-tables were computed according to ref. 77, using the data presented in refs. 78, 79, and 80, respectively. The H^- bound-free and free-free opacities were calculated according to ref. 81. Also included were e^- and H, both assumed to be well-mixed with abundances fixed to the deep atmosphere H^- abundance. The latter was justified because the abundances of e^- and H do not affect the observed emission spectrum provided that the abundances are sufficiently high to allow significant interaction with the H^- ions. Collision-induced absorption due to H_2–H_2 and H_2–He was also included.[82-86] A parameterisation identical to that used by the ATMO retrievals was adopted for the PT profile. At each orbital phase, this gave a final model with seven free parameters: three parameters for the PT profile (κ_{IR}, γ, ψ); the H^- mole fraction; and the three parameters defined above for the pressure-dependent H_2O mole fraction (X_{deep}, P_{knee}, α).

Results for the fiducial dayside and nightside hemisphere PT profiles, H_2O abundances, and H^- abundances are compared to those obtained by the ATMO retrievals in Extended Data Fig. 8. Maximum likelihood emission spectra are shown for all orbital phases in Extended Data Fig. 4, with the PT profiles, H_2O abundances, and H^- abundances that were retrieved separately for each phase shown in Extended Data Figs 5, 6, and 7, respectively. Overall, the PT profiles inferred by NEMESIS for the nightside phases are in good agreement with those inferred by ATMO. The agreement is reasonable, but not as good, for the dayside phases. The latter is likely due to the challenge of accounting for thermal dissociation and ionisation using the parameterised approach described above for the free chemistry NEMESIS retrievals. The NEMESIS retrievals at dayside phases do not succeed in accounting for the thermal dissociation of H_2O (Extended Data Fig. 8b). Instead, to account for the muted H_2O spectral band, the NEMESIS retrieval favours a higher H^- abundance compared to ATMO (Extended Data Fig. 8c), which raises the opacity at wavelengths shortward of 1.3μm in particular (Extended Data Fig. 3). The overall raised opacity produces an extended wing in the contribution function towards lower pressures (Extended Data Fig. 8d), in turn favouring a thermal inversion at lower pressures than ATMO (Extended Data Fig. 8a). This also explains why NEMESIS infers thermal inversions at lower pressures than ATMO for phases ϕ = 0.43, 0.57, and 0.62 (Extended Data Fig. 5).

However, the broad agreement between the NEMESIS and ATMO results is reassuring, given the different methodologies adopted. The NEMESIS χ^2 fit statistics are reported alongside those for ATMO in Extended Data Table 8. For NEMESIS, the mean reduced $\chi_v^2 = 2.43$ and the median reduced $\chi_v^2 = 2.34$, which are significantly higher than the equivalent fit quality metrics achieved by ATMO. This is primarily a consequence of the larger number of parameters required for the NEMESIS retrievals (i.e. seven for NEMESIS versus three for ATMO), although the

absolute χ^2 values are also higher, indicating that the NEMESIS models do not replicate the data as well as the ATMO models overall. The latter is due to the failure of NEMESIS to adequately treat the thermal dissociation of H_2O for the dayside spectra, as noted above. For these reasons, along with the physically-motivated enforcement of chemical equilibrium, we present the ATMO retrievals as our primary analysis (Figs 2 and 3).

General circulation models

A three-dimensional general circulation model (GCM) simulation was performed for the atmosphere of WASP-121b using the Substellar and Planetary Radiation and Circulation (SPARC) model.[87-95] The model couples the MITgcm dynamical core,[96] a finite-volume code that solves the three-dimensional primitive equations on a staggered Arakawa C grid,[97] with a plane-parallel, two-stream version of a multi-stream radiation code developed for planetary atmospheres.[98] Opacities are calculated using the correlated-*k* method[99] assuming local thermodynamic and chemical equilibrium for each PT point, using the solar photospheric elemental abundances of ref. 100. In particular, the model includes opacity due to important absorbers such as H_2O, H^-, CO, TiO, and VO, but does not yet include atomic metals such as Fe and Mg. The coupling of the dynamical core and radiative transfer scheme allow for the self-consistent calculation of the heating and cooling rates of the atmosphere.

The SPARC GCM for WASP-121b has a horizontal resolution of C32 (128×64 in longitude and latitude, respectively) and a vertical resolution of 45 pressure levels evenly spaced in log pressure, that extend from a mean pressure of 1,000 bar at the bottom to 200 μbar at the top. The model was integrated for 80 Earth days (~60 planetary orbits). A global map of the temperature and wind speeds at a pressure of 10 mbar (a pressure within the range of altitudes probed at the

WFC3 wavelengths, e.g. Fig. 3d) is shown in Extended Data Fig. 13. The map shows predominantly eastward flow at the equator and nightside vortices, with dayside temperatures exceeding 3,000 Kelvin and nightside temperatures dropping to ~1,000 Kelvin. Synthetic phase curves were generated from the GCM following refs 24 and 101, and are shown in Fig. 1 and Extended Data Fig. 2. Predicted emission spectra are shown in Fig. 2 and Extended Data Fig. 4. Also shown in the latter figures are predicted emission spectra from the independent GCM simulations of ref. 10, which were performed for atmospheric metallicities of 1x and 5x solar.

Two important caveats are worth highlighting, which apply to the GCM simulation presented here, as well as those published by ref. 10. First, the lack of opacity due to metals such as Fe and Mg could be significant, as separate modelling has shown that these metals can play major roles in determining the outgoing emission for ultrahot Jupiters such as WASP-121b.[11] Second, the atmosphere of WASP-121b was assumed to be cloud-free to simplify the modelling. However, clouds could potentially play a significant role in the atmospheric radiative transfer for WASP-121b, particularly on the nightside hemisphere and in the terminator region where temperatures are relatively low and likely conducive to the condensation of numerous species (Fig. 3b).

Data availability

Raw HST data frames are publicly available online at the Mikulski Archive for Space Telescopes (MAST; https://archive.stsci.edu).

Code availability

The main analysis routines have been written by the authors in Python and are available on request. Other publicly available code that was used has been cited throughout the text.

Methods References

41. Stevenson, K. B., Fowler, J. Analysing Eight Years of Transiting Exoplanet Observations Using WFC3's Spatial Scan Monitor. *Space Telescope Science Institute WFC3 Instrument Science Report*. 2019-12 (2019).
42. Evans, T. M. et al. Detection of H- and Evidence for TiO/VO in an Ultra-hot Exoplanet Atmosphere. *Astrophys. J*. 822, (2016).
43. Evans, T. M. et al. An ultrahot gas-giant exoplanet with a stratosphere. *Nature*. 548, (2017).
44. Mikal-Evans et al. An emission spectrum for WASP-121b measured across the 0.8-1.1μm wavelength range using the Hubble Space Telescope. *Mon. Not. R. Astron. Soc*. 488, (2019).
45. de Wit, J. et al. Atmospheric reconnaissance of the habitable-zone Earth-sized planets orbiting TRAPPIST-1. *Nature Astron*. 2, (2018).
46. Kreidberg, L. batman: BAsic Transit Model cAlculatioN in Python. *Publ. Astron. Soc. Pac*. 127, (2015).
47. Foreman-Mackey, D., Hogg, D. W., Lang, D., Goodman, J. emcee: The MCMC Hammer. *Publ. Astron. Soc. Pac*. 125, (2013).
48. Parmentier, V. & Crossfield, I. J. M. Exoplanet phase curves: observations and theory. *Handbook of Exoplanets*, ed. Deeg, H. J. & Belmonte, J. A. Springer Publishing, Cham (2018).
49. Louden, T., Kreidberg, L. SPIDERMAN: an open-source code to model phase curves and secondary eclipses. *Mon. Not. R. Astron. Soc*. 477, (2018).

50. Deming, D. et al. Infrared Transmission Spectroscopy of the Exoplanets HD 209458b and XO-1b Using the Wide Field Camera-3 on the Hubble Space Telescope. *Astrophys. J*. 774, (2013).

51. Tremblin, P. et al. Fingering Convection and Cloudless Models for Cool Brown Dwarf Atmospheres. *Astrophys. J*. 804, (2015).

52. Tremblin, P. et al. Cloudless Atmospheres for L/T Dwarfs and Extrasolar Giant Planets. *Astrophys. J*. 817, (2016).

53. Tremblin, P. et al. Advection of Potential Temperature in the Atmosphere of Irradiated Exoplanets: A Robust Mechanism to Explain Radius Inflation. *Astrophys. J*. 841, (2017).

54. Tremblin, P. et al. Cloudless Atmospheres for Young Low-gravity Substellar Objects. *Astrophys. J*. 850, (2017).

55. Amundsen, D. S. et al. Accuracy tests of radiation schemes used in hot Jupiter global circulation models. *Astron. Astrophys*. 564, (2014).

56. Drummond, B. et al. The effects of consistent chemical kinetics calculations on the pressure-temperature profiles and emission spectra of hot Jupiters. *Astron. Astrophys*. 594, (2016).

57. Goyal, J. M. et al. A library of ATMO forward model transmission spectra for hot Jupiter exoplanets. *Mon. Not. R. Astron. Soc*. 474, (2018).

58. Goyal, J. M. et al. Fully scalable forward model grid of exoplanet transmission spectra. *Mon. Not. R. Astron. Soc*. 482, (2019).

59. Goyal, J. M. et al. A library of self-consistent simulated exoplanet atmospheres. *Mon. Not. R. Astron. Soc*. 498, 4680 (2020).

60. Phillips, M. W. et al. A new set of atmosphere and evolution models for cool T-Y brown dwarfs and giant exoplanets. *Astron. Astrophys*. 637, (2020).

61. Guillot, T. On the radiative equilibrium of irradiated planetary atmospheres. *Astron. Astrophys*. 520, A27 (2010).

62. Feroz, F., Hobson, M. P. Multimodal nested sampling: an efficient and robust alternative to Markov Chain Monte Carlo methods for astronomical data analyses. *Mon. Not. R. Astron. Soc*. 384, (2008).

63. Feroz, F., Hobson, M. P., Bridges, M. MULTINEST: an efficient and robust Bayesian inference tool for cosmology and particle physics. *Mon. Not. R. Astron. Soc*. 398, (2009).

64. Feroz, F., Hobson, M. P., Cameron, E., Pettitt, A. N. Importance Nested Sampling and the MultiNest Algorithm. *Open J. Astrophys*. 2, (2019).

65. Castelli, F. & Kurucz, R. L. New grids of ATLAS9 model atmospheres. Preprint at https://arxiv.org/abs/astro-ph/0405087 (2004).

66. Kass, R. E. & Raftery, E. Bayes factors. *J. Am. Stat. Assoc.* 90, 773 (1995).

67. Jeffreys, H. *The Theory of Probability (3rd ed.)*. Oxford Univ. Press, Oxford (1998).

68. Trotta, R. Bayes in the sky: Bayesian inference and model selection in cosmology. *Contemp. Phys.* 49, 71 (2008).

69. Cowan, N. B., Agol, E. The statistics of albedo and heat recirculation of hot exoplanets. *Astrophys. J.* 729, 54 (2011).

70. Keating, D., Cowan, N. B., Dang, L. Uniformly hot nightside temperatures on short-period gas giants. *Nat. Astro.* 3, 1092 (2019).

71. Perna, R., Menou, K., Rauscher, E. Magnetic Drag on Hot Jupiter Atmospheric Winds. *Astrophys. J.* 719, 1421 (2010).

72. Batygin, K., Stanley, S., Stevenson, D. J. Magnetically controlled circulation on hot extrasolar planets. *Astrophys. J.* 776, 53 (2013).

73. Irwin, P. G. J. et al. The NEMESIS planetary atmosphere radiative transfer and retrieval tool. *J. Quant. Spectrosc. Radiat. Transf.* 109, (2008).

74. Lee, J.-M., Fletcher, L. N., Irwin, P. G. J. Optimal estimation retrievals of the atmospheric structure and composition of HD 189733b from secondary eclipse spectroscopy. *Mon. Not. R. Astron. Soc*. 420, (2012).

75. Barstow, J. K., Aigrain, S., Irwin, P. G. J., Sing, D. K. A Consistent Retrieval Analysis of 10 Hot Jupiters Observed in Transmission. *Astrophys. J*. 834, (2017).

76. Krissansen-Totton, J., Garland, R., Irwin, P., Catling, D. C. Detectability of Biosignatures in Anoxic Atmospheres with the James Webb Space Telescope: A TRAPPIST-1e Case Study. *Astron. J*. 156, (2018).

77. Buchner, J. et al. X-ray spectral modelling of the AGN obscuring region in the CDFS: Bayesian model selection and catalogue. *Astron. Astrophys*. 564, (2014).

78. Lacis, A. A., Oinas, V. A description of the correlated-k distribution method for modelling nongray gaseous absorption, thermal emission, and multiple scattering in vertically inhomogeneous atmospheres. *J. Geophys. Res*. 96, 9027 (1991).

79. Chubb, K. L. et al. The ExoMolOP Database: Cross-sections and k-tables for Molecules of Interest in High-Temperature Exoplanet Atmospheres. Preprint at https://arxiv.org/abs/2009.00687 (2020).

80. Polyansky, O. L. et al. ExoMol molecular line lists XXX: a complete high-accuracy line list for water. *Mon. Not. R. Astron. Soc*. 480, (2018).

81. McKemmish, L. K., Yurchenko, S. N., Tennyson, J. ExoMol line lists – XVIII. The high-temperature spectrum of VO. *Mon. Not. R. Astron. Soc*. 463, 771 (2016).

82. Wende, S., Reiners, A., Seifahrt, A., Bernath, P. F. CRIRES spectroscopy and empirical line-by-line identification of FeH molecular absorption in an M dwarf. *Astron. Astrophys*. 523, A58 (2010).

83. John, T. L. Continuous absorption by the negative hydrogen ion reconsidered. *Astron. Astrophys*. 193, 189 (1988).

84. Borysow, A. Collision-induced absorption coefficients of H2 pairs at temperatures from 60 K to 1000 K. *Astron. Astrophys*. 390, 779 (2002).

85. Borysow, A., Frommhold, L. Collision-induced Infrared Spectra of H 2-He Pairs at Temperatures from 18 to 7000 K. II. Overtone and Hot Bands. *Astrophys. J*. 341, (1989).

86. Borysow, A., Frommhold, L. A New Computation of the Infrared Absorption by H 2 Pairs in the Fundamental Band at Temperatures from 600 to 5000 K. *Astrophys. J*. 348, (1990).

87. Borysow, A., Frommhold, L., Moraldi, M. Collision-induced Infrared Spectra of H 2-He Pairs Involving 0 1 Vibrational Transitions and Temperatures from 18 to 7000 K. *Astrophys. J*. 336, (1989).

88. Borysow, A., Jorgensen, U. G., Fu, Y. High-temperature (1000-7000 K) collision-induced absorption of H"2 pairs computed from the first principles, with application to cool and dense stellar atmospheres. *J. Quant. Spectrosc. Radiat. Transf*. 68, (2001).

89. Showman, Adam P. et al. Atmospheric Circulation of Hot Jupiters: Coupled Radiative-Dynamical General Circulation Model Simulations of HD 189733b and HD 209458b. *Astrophys. J*. 699, (2009).

90. Showman, A. P., Fortney, J. J., Lewis, N. K., Shabram, M. Doppler Signatures of the Atmospheric Circulation on Hot Jupiters. *Astrophys. J*. 762, (2013).

91. Showman, A. P., Lewis, N. K., Fortney, J. J. 3D Atmospheric Circulation of Warm and Hot Jupiters. *Astrophys. J*. 801, (2015).

92. Kataria, T. et al. Three-dimensional Atmospheric Circulation of Hot Jupiters on Highly Eccentric Orbits. *Astrophys. J*. 767, (2013).

93. Kataria, T., Showman, A. P., Fortney, J. J., Marley, M. S., Freedman, R. S. The Atmospheric Circulation of the Super Earth GJ 1214b: Dependence on Composition and Metallicity. *Astrophys. J*. 785, (2014).
94. Kataria, T. et al. The Atmospheric Circulation of the Hot Jupiter WASP-43b: Comparing Three-dimensional Models to Spectrophotometric Data. *Astrophys. J*. 801, (2015).
95. Kataria, T. et al. The Atmospheric Circulation of a Nine-hot-Jupiter Sample: Probing Circulation and Chemistry over a Wide Phase Space. *Astrophys. J*. 821, (2016).
96. Lewis, Nikole K. et al. Atmospheric Circulation of Eccentric Hot Neptune GJ436b. *Astrophys. J*. 720, (2010).
97. Lewis, N. K., Showman, A. P., Fortney, J. J., Knutson, H. A., Marley, M. S. Atmospheric Circulation of Eccentric Hot Jupiter HAT-P-2b. *Astrophys. J*. 795, (2014).
98. Adcroft, A., Campin, J.-M., Hill, C., Marshall, J. Implementation of an Atmosphere Ocean General Circulation Model on the Expanded Spherical Cube. *Mon. Weather Rev*. 132, 2845 (2004).
99. Arakawa, A., Lamb, V. R. Computational design of the basic dynamical processes of the UCLA general circulation model. *Methods in Computational Physics: Advances in Research and Applications*. 17, 173 (1977).
100. Marley, M. S., McKay, C. P. Thermal Structure of Uranus' Atmosphere. *Icarus*. 138, 268 (1999).
101. Goody, R. M., Yung, Y. L. Atmospheric radiation: Theoretical basis. Oxford University Press, New York/Oxford (1989).
102. Lodders, K. Solar System Abundances and Condensation Temperatures of the Elements. Astrophys. J. 591, 1220 (2003).
103. Fortney, J. J., Cooper, C. S., Showman, A. P., Marley, M. S., Freedman, R. S. The Influence of Atmospheric Dynamics on the Infrared Spectra and Light Curves of Hot Jupiters. *Astrophys. J*. 652, (2006).

Acknowledgements

Support for HST program GO-15134 was provided by NASA through a grant from the Space Telescope Science Institute, which is operated by the Association of Universities for Research in Astronomy, Inc., under NASA contract NAS 5-26555. N.M. is supported by a UKRI Future Leaders Fellowship: MR/T040866/1, a Science and Technology Facilities Council Consolidated Grant (ST/R000395/1) and the Leverhulme Trust through a research project grant (RPG-2020-82).

Author Contributions

T.M.E. co-led the observing program, analysed the HST data, and wrote the manuscript. D.K.S., J.K.B, and J.T. performed the retrieval analyses. T.K. co-led the observing program and ran the GCM simulation. J.G. and N.L. processed the GCM results. T. D. assisted with the light curve analysis. All authors discussed the results and provided feedback on the manuscript.

Competing Interest Declaration

The authors declare no competing interests.

EXTENDED DATA

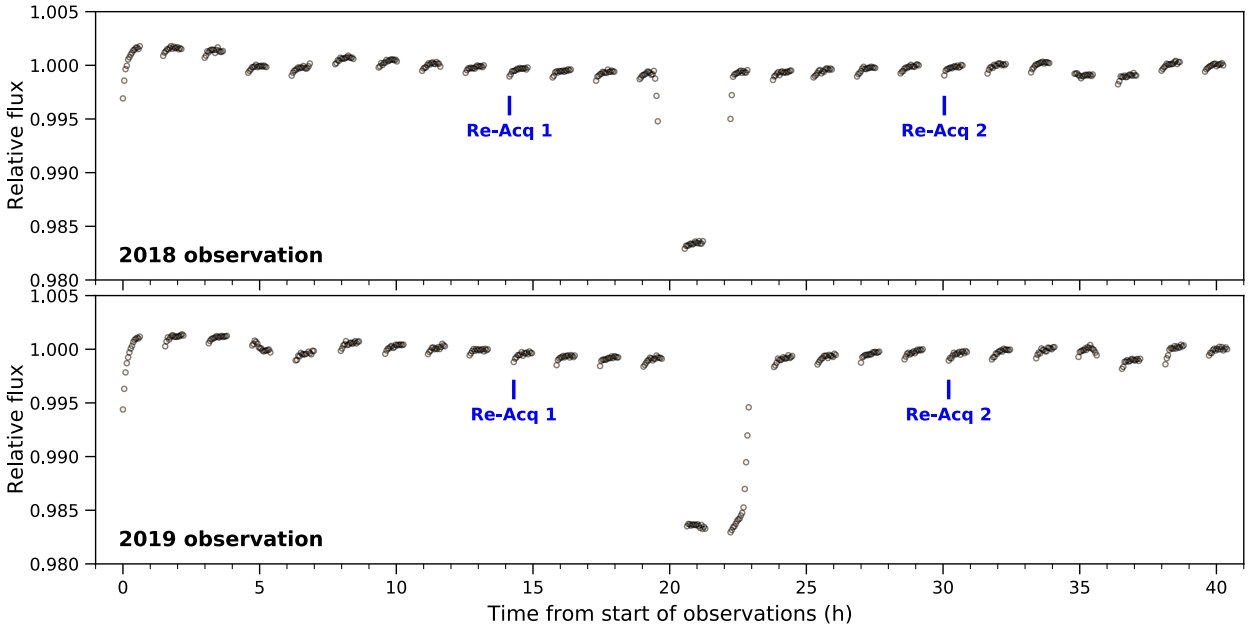

Extended Data Fig. 1. Raw broadband light curves for WASP-121b. WFC3 observations made in 2018 and 2019. Gaps in the time series are due to the target disappearing from view for approximately half of each HST orbit. Two secondary eclipses and the primary transit are visible by eye. The data are affected by detector systematics that result in a ramp-up of flux registered during each HST orbit. Guide star re-acquisitions were performed at the beginning of the 10th and 20th HST orbits for both observations.

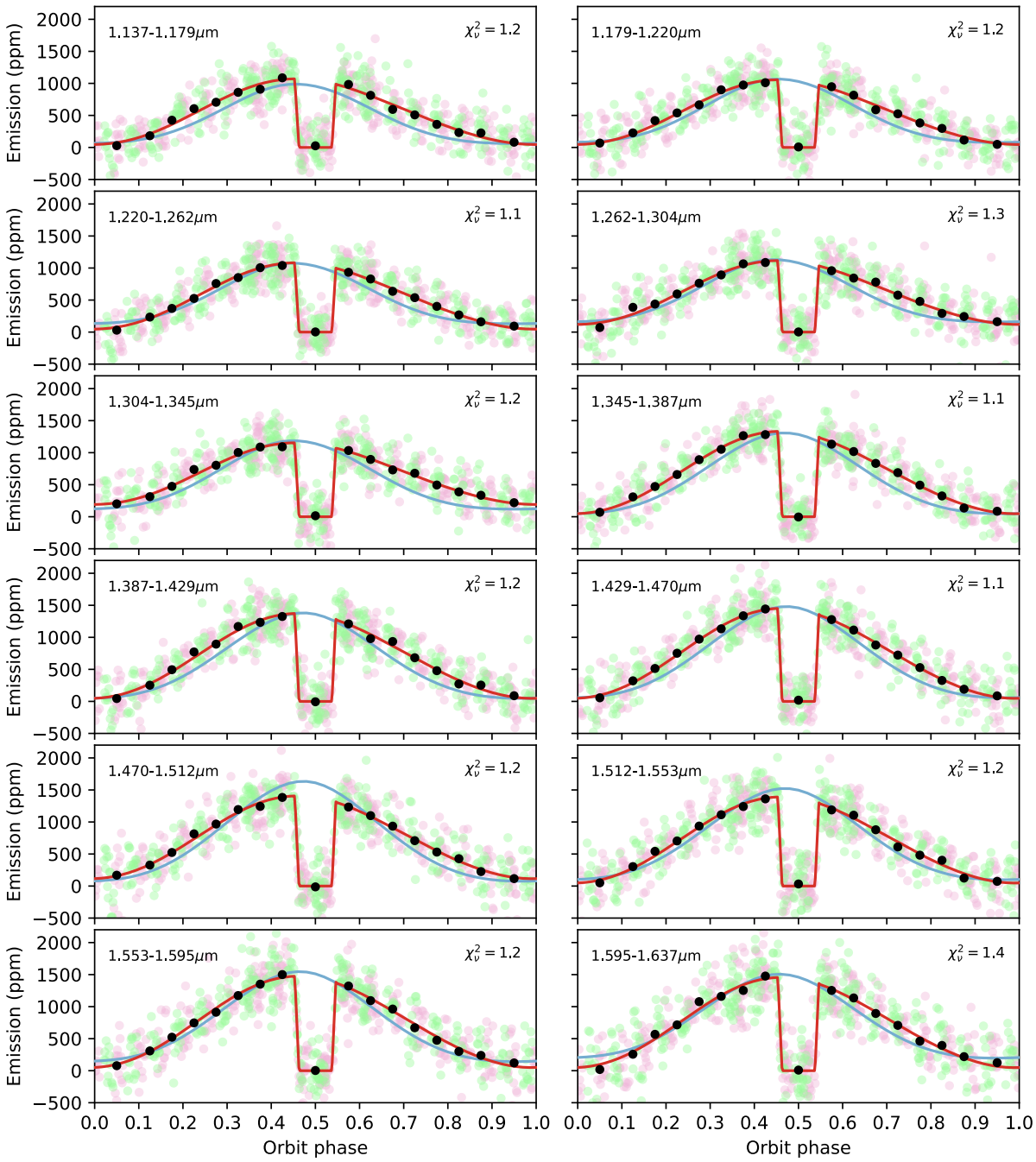

Extended Data Fig. 2. Spectroscopic phase curves for WASP-121b. Systematics-corrected spectroscopic phase curves measured with WFC3. Pink circles show 2018 data and green circles show 2019 data. Black circles show the combined dataset binned in phase, with marker sizes approximately corresponding to the measurement uncertainties. Phase bins are the same as those used for generating the phase-resolved emission spectra, plus an additional in-eclipse bin. Red lines show the maximum likelihood second-order sinusoidal fits, with corresponding reduced χ^2_ν values listed in the upper right corner of each axis. Blue lines show predictions of the 3D GCM run for the present study.

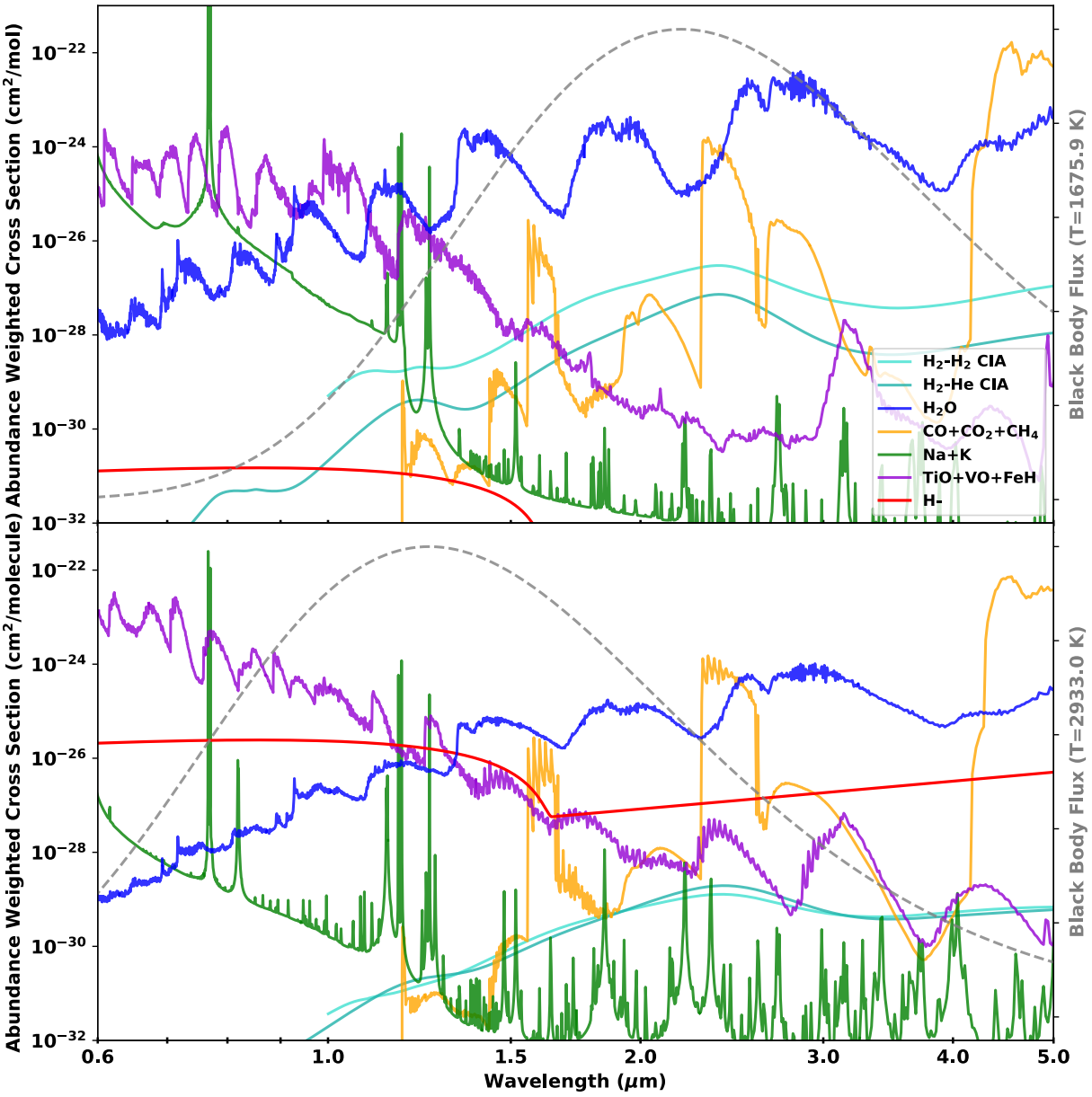

Extended Data Fig. 3. Spectrally active gases on the nightside (top panel) and dayside (bottom panel) hemispheres. Solid lines show absorption cross-sections for spectrally active species weighted by their mole fractions at pressures just below the contribution function peaks, as inferred by the ATMO "2x PT" retrieval analyses. Dashed grey lines show blackbody emission curves for the retrieved temperatures at the same pressure levels.

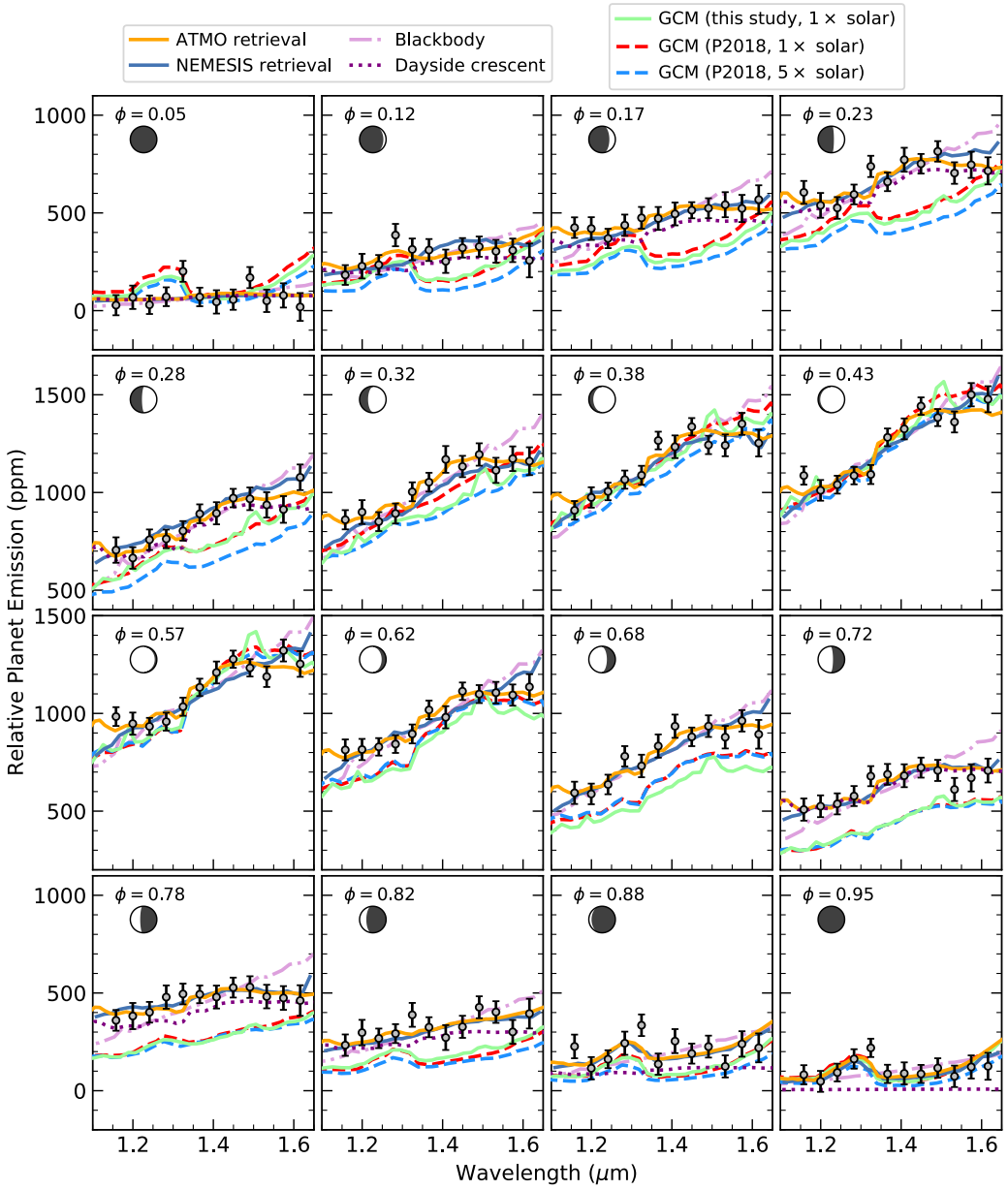

Extended Data Fig. 4. Emission spectra at different orbital phases for WASP-121b. Grey circles show measured planet emission as a function of wavelength with error bars indicating 1σ measurement uncertainties. Solid orange and dark blue lines show the maximum likelihood spectra obtained from the ATMO "2x PT" retrievals and NEMESIS "2x PT" retrievals, respectively. Dotted purple lines show dayside contributions for the phases at which retrievals were performed for the nightside emission. Solid light green line shows the emission predicted by the 3D GCM run for the present study assuming 1x solar metallicity. Dashed red and blue lines show the emission predicted by the 3D GCM simulations of ref 10 assuming 1x and 5x solar metallicity, respectively. Dot-dashed purple lines show best-fit blackbody spectra. Circle symbols indicate the illuminated fraction of the visible hemisphere at each orbital phase.

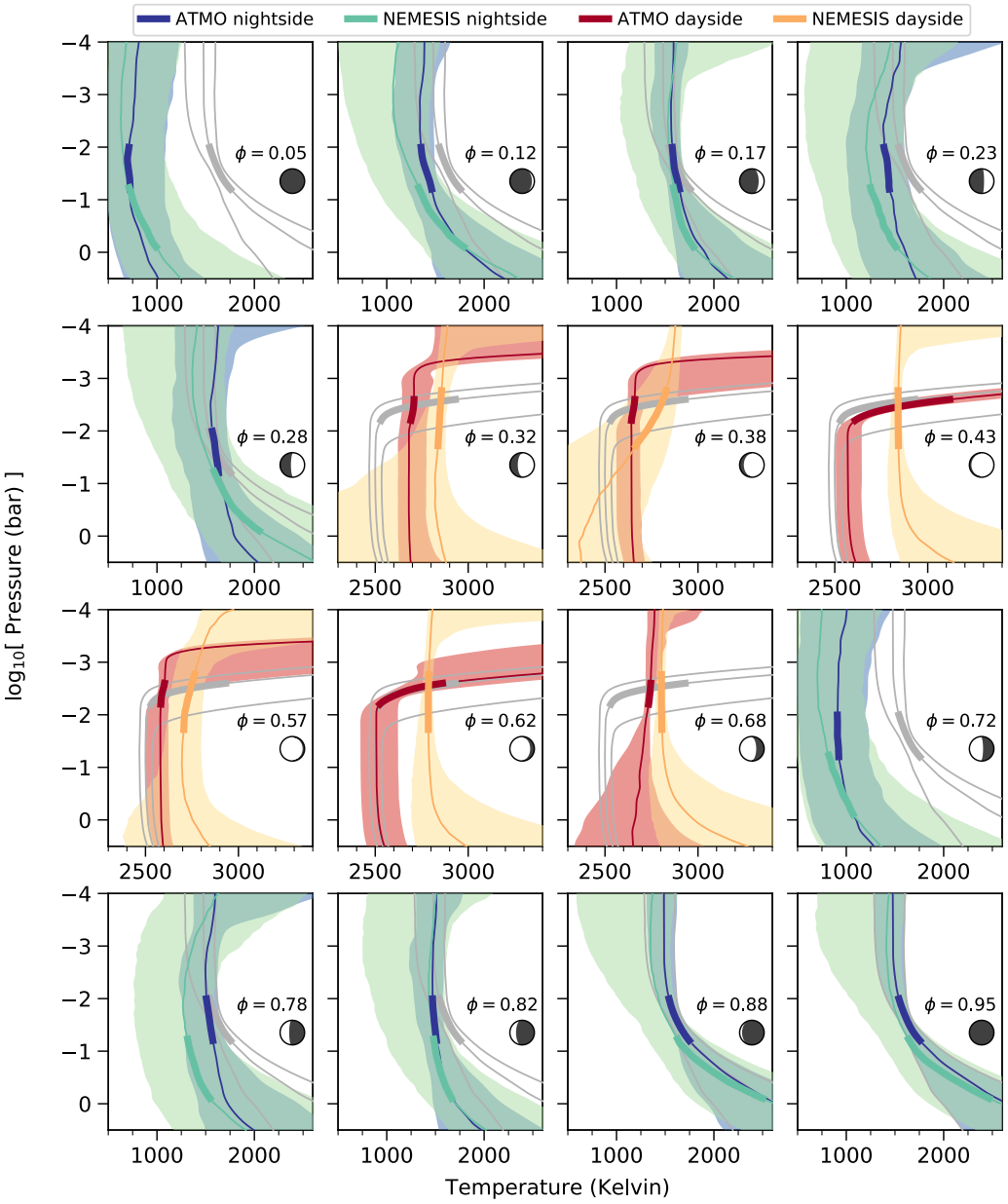

Extended Data Fig. 5. Pressure-temperature (PT) profiles retrieved for different orbital phases. Blue lines show the median PT profiles obtained from the ATMO "2x PT" nightside retrievals, with blue shading the corresponding 1σ credible ranges. Red lines and shading show the same for the ATMO "2x PT" dayside retrievals. Green and yellow lines and shading show the same for the NEMESIS "2x PT" nightside and dayside retrievals, respectively. For the ATMO retrievals, thick lines correspond to the same pressures highlighted in Fig. 3, where the contribution function is greatest. For the NEMESIS retrievals, thick lines indicate the equivalent pressures of greatest contribution for those retrievals (Extended Data Fig. 8d). Grey lines reproduce the fiducial dayside and nightside PT distributions of Fig. 3.

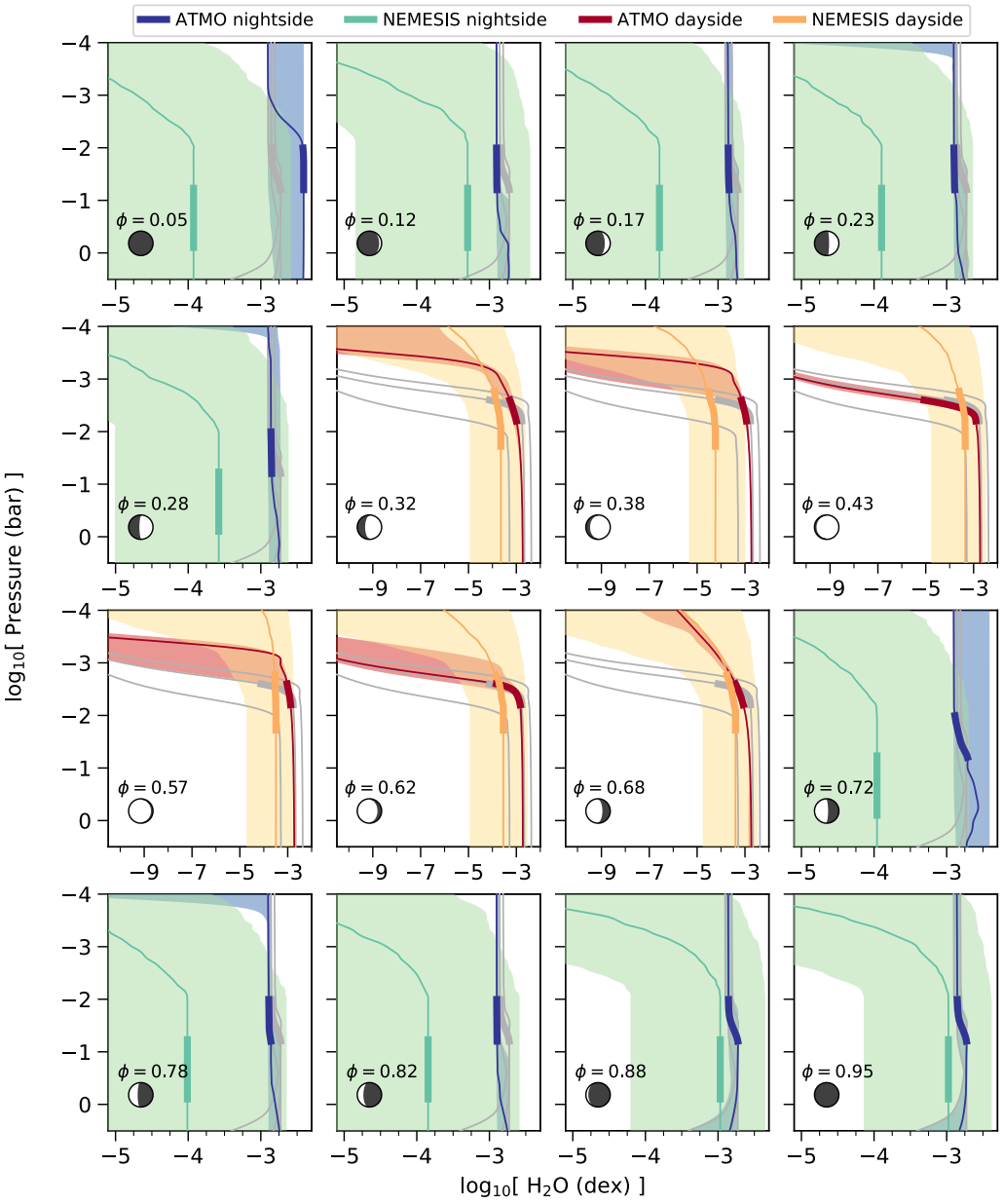

Extended Data Fig. 6. Retrieved pressure-dependent H_2O abundances. Same format as Extended Data Figure 5, but showing posterior distributions for the retrieved H_2O abundances. ATMO credible ranges are much narrower than those of NEMESIS, due to the metallicity being fixed for the ATMO retrievals whereas the H_2O abundance was unconstrained for the NEMESIS retrievals.

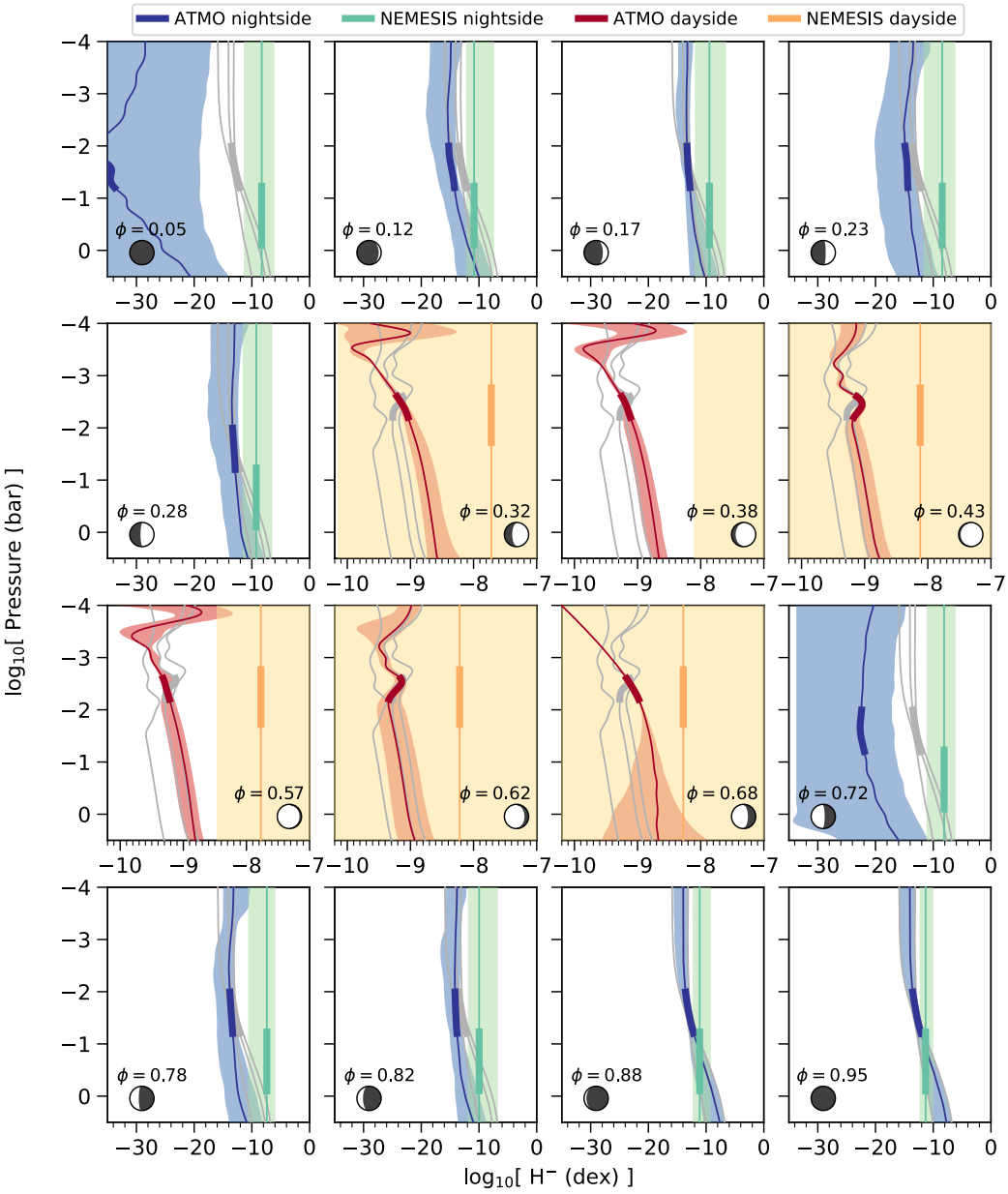

Extended Data Fig. 7. Retrieved pressure-dependent H^- abundances. Same format as Extended Data Figs 5 and 6, but showing posterior distributions for the retrieved H^- abundances.

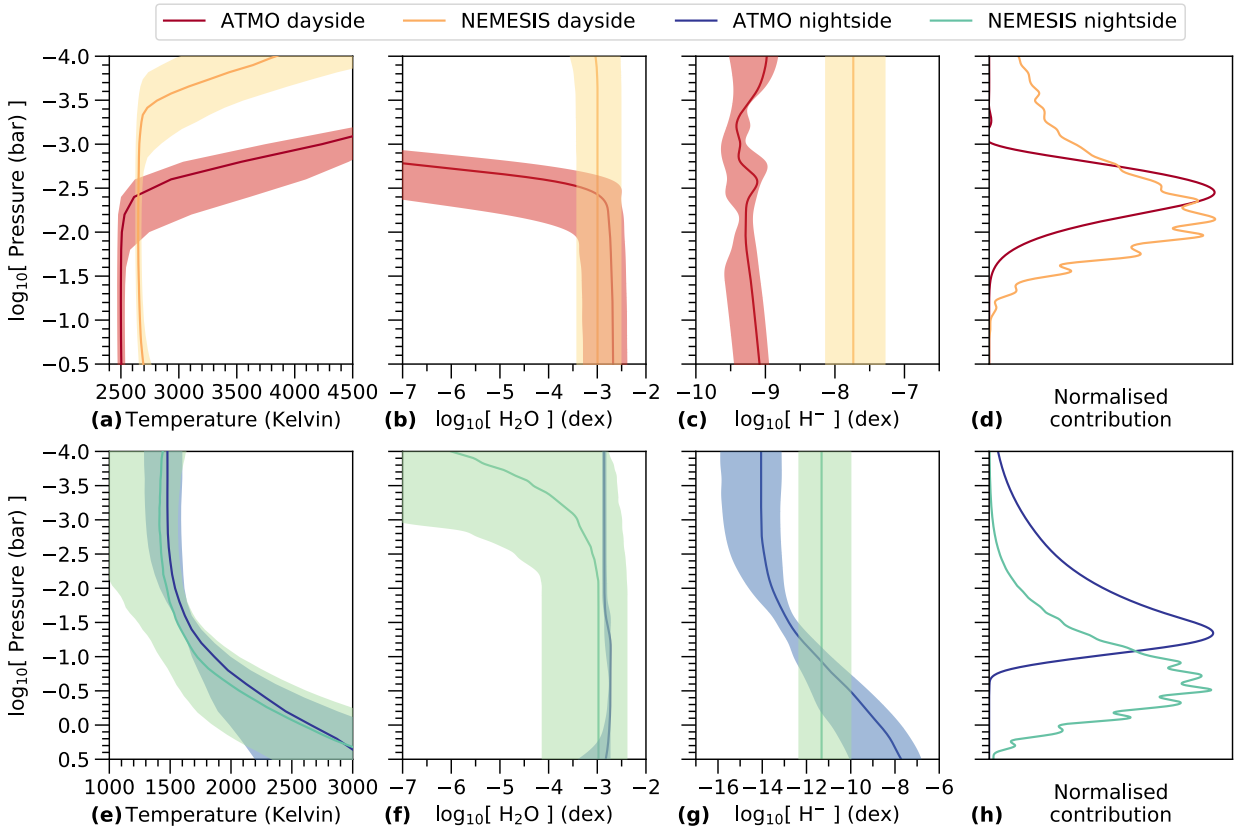

Extended Data Fig. 8. ATMO and NEMESIS "2x PT" retrievals for the fiducial dayside and nightside spectra. Top panel shows (from left to right) the retrieved PT profiles, H_2O abundances, H^- abundances, and normalised contribution functions for the fiducial dayside spectrum. Bottom panel shows the same for the fiducial nightside spectrum. Same colour scheme as Extended Data Figs 5-7.

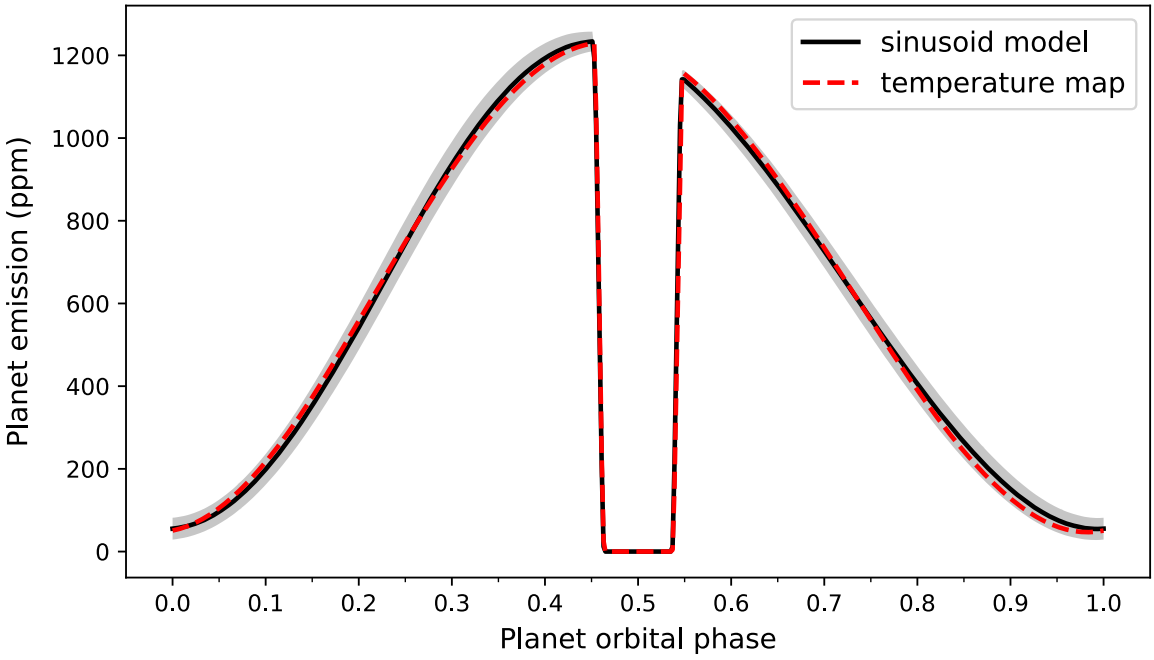

Extended Data Fig. 9. Phase curve models for the broadband planet emission of WASP-121b. Black solid line shows the median of the second-order sinusoidal models sampled by the MCMC light curve analysis and grey shading shows the corresponding standard deviation. Dashed red line shows a light curve generated by the third-order spherical harmonics temperature map described in Methods, optimised to match the second-order sinusoidal model.

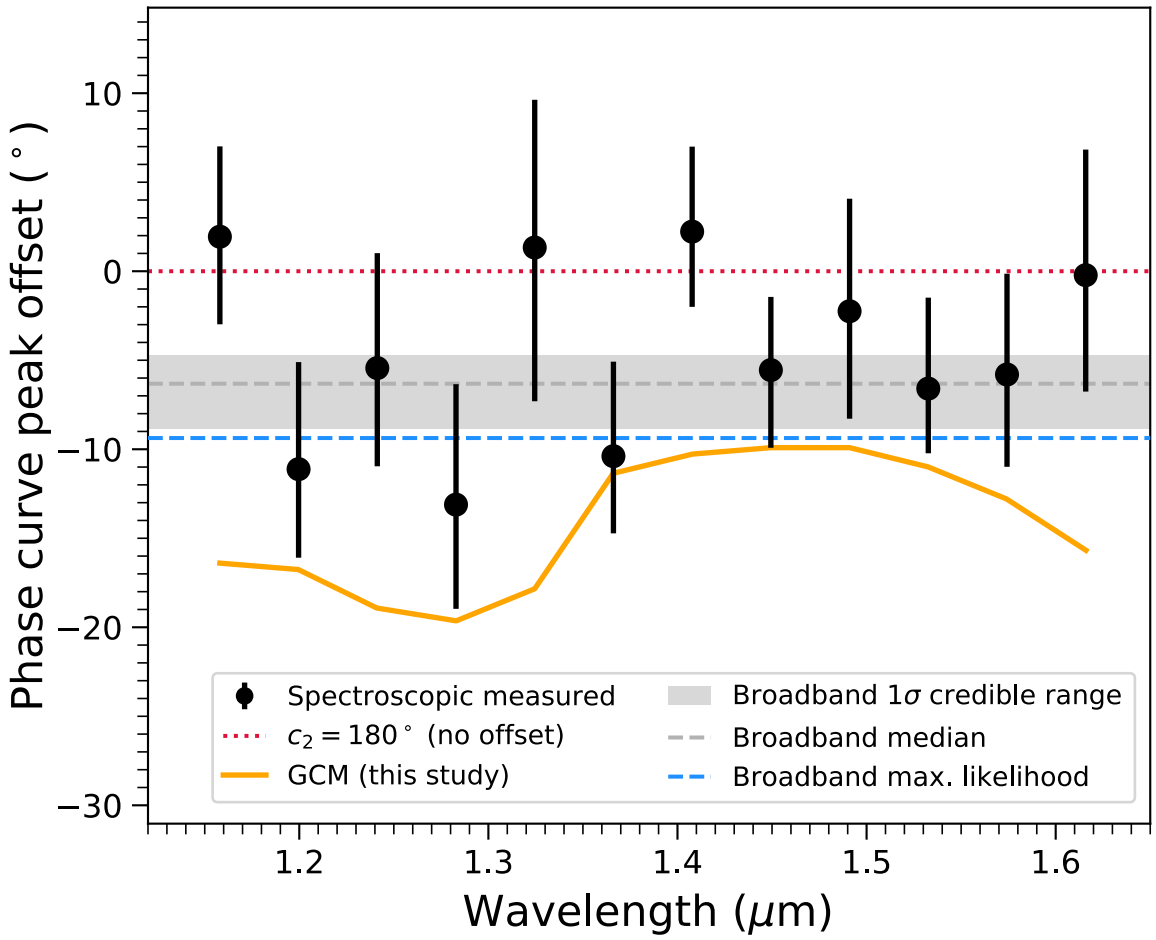

Extended Data Fig. 10. Phase curve peak offset as a function of wavelength. Black circles show posterior medians for c_2–π (i.e. hot spot phase offset) obtained for each spectroscopic light curve fit, expressed in units of degrees, with error bars showing the 1σ credible ranges. Dotted red line corresponds to the zero point of c_2=π radian (i.e. ϕ=0.5). Dashed grey line shows the posterior median obtained for the broadband light curve fit, with grey shading indicating the 1σ credible range. Dashed blue line corresponds to the maximum likelihood value of c_2=2.98 radian obtained for the broadband light curve and held fixed for the final spectroscopic light curve fits. Solid orange line shows the phase curve peak offsets predicted by the GCM run for this study, assuming an atmospheric metallicity of 1x solar and no atmospheric drag.

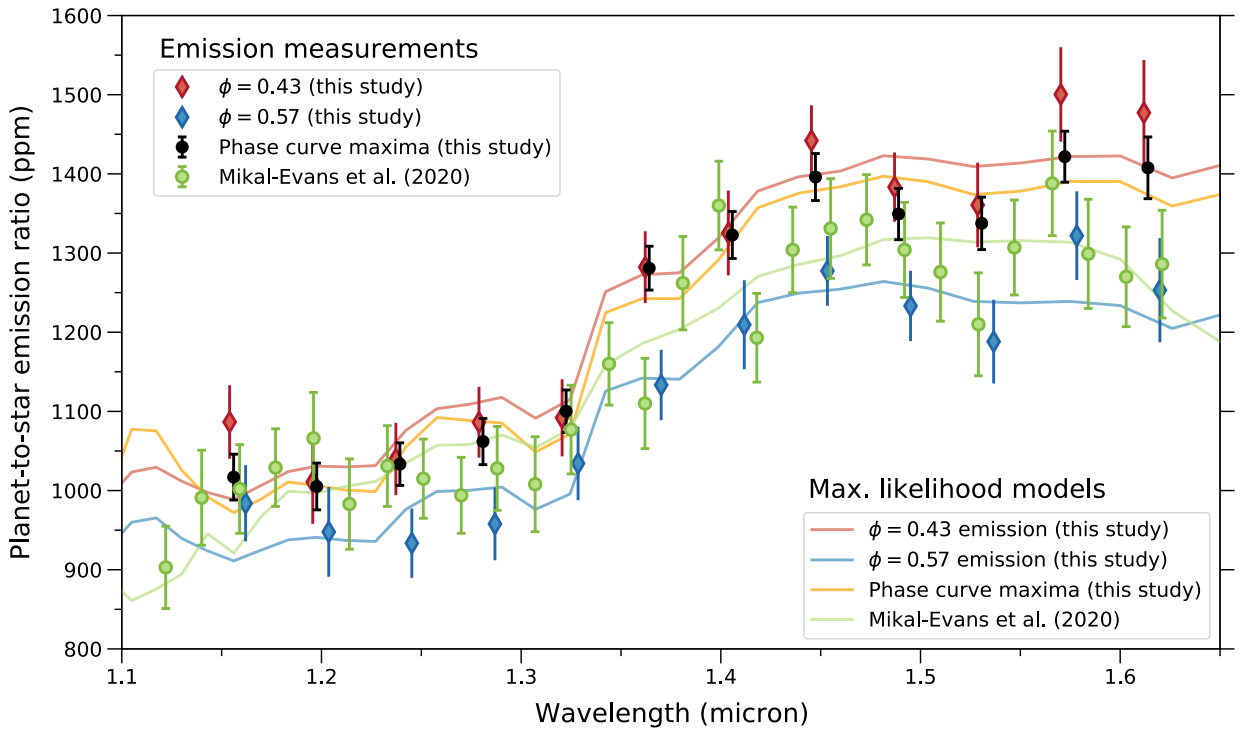

Extended Data Fig. 11. Emission spectrum of the WASP-121b dayside hemisphere. Black circles show the medians of the phase curve maxima sampled during spectroscopic light curve fitting with 1σ error bars. Red and blue diamonds show the binned planetary flux at orbital phases ϕ=0.43 and ϕ=0.57, respectively, with 1σ error bars. Green circles show the secondary eclipse spectrum published in ref. 3 with 1σ error bars. Solid lines show the maximum likelihood models for each dataset with colour scheme described in the legend.

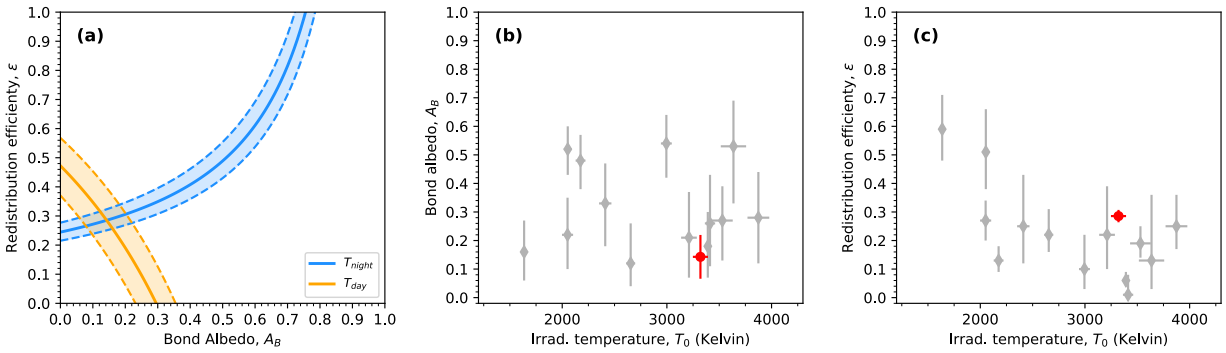

Extended Data Fig. 12. Bond albedo and heat redistribution efficiencies for WASP-121b and other irradiated substellar objects. a, Constraints obtained for the Bond albedo and heat redistribution efficiency from the dayside brightness temperature ($T_{\rm day}$) and nightside brightness temperature ($T_{\rm night}$), following the method of ref. 67. **b,** Grey diamonds show Bond albedos A_B for an ensemble of irradiated substellar objects reported by ref. 68 as a function of the irradiation temperature, $T_0 = T_\star\sqrt{R_\star/a}$. Red circle shows the result for WASP-121b obtained in the present study. Error bars give 1σ uncertainties. **c,** The same as **b** but showing the inferred heat redistribution efficiency values ε as a function of irradiation temperature.

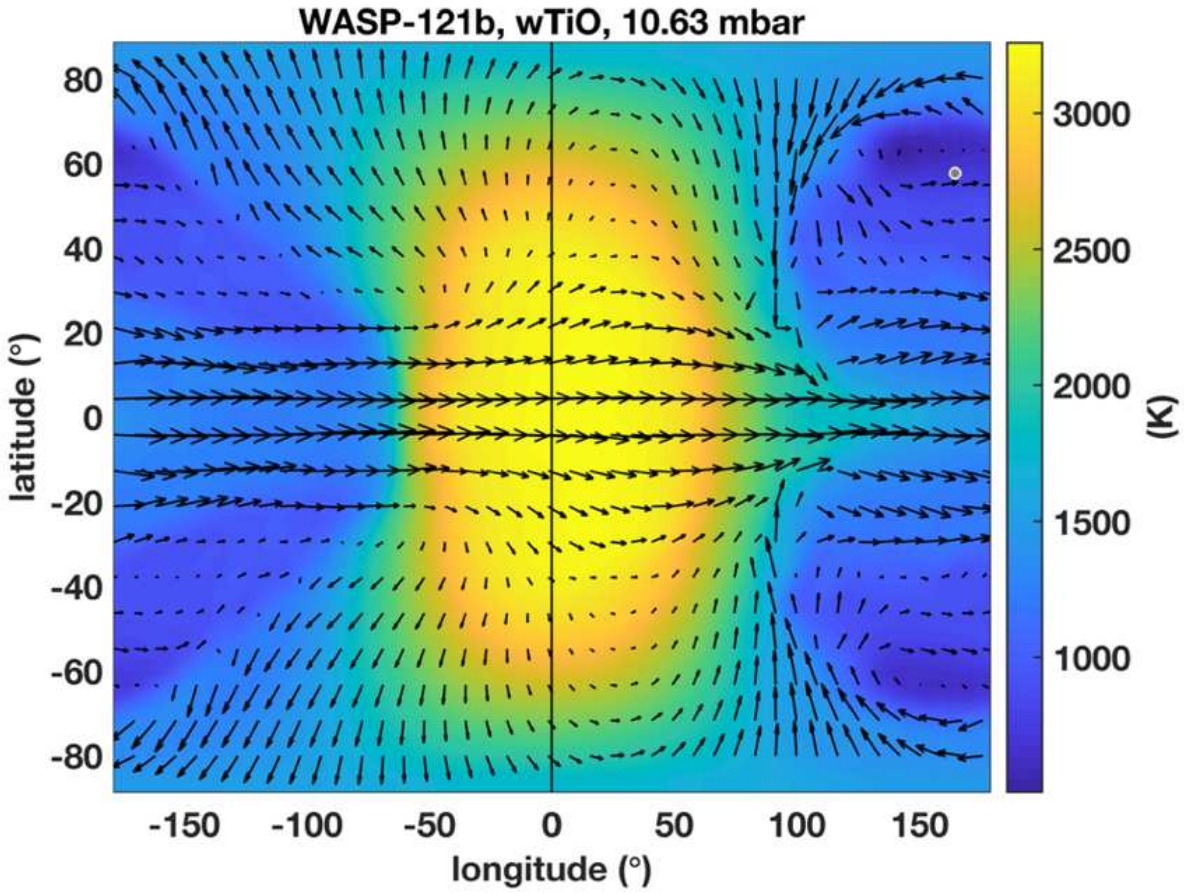

Extended Data Fig. 13. General circulation model for WASP-121b. Temperature (colour scale in Kelvin) and winds (arrows) for the SPARC GCM simulation of WASP-121b run for the present study, assuming 1× solar metallicity, chemical equilibrium, and no atmospheric drag. The vertical black line indicates the substellar longitude.

Extended Data Table 1. Astrophysical parameters obtained from fits to the broadband light curve. Results are reported for fits adopting first-order and second-order sinusoidal models for the planetary phase variations. Values listed for free parameters are posterior medians and uncertainties give the 1σ credible ranges. Note that inclination i values have been derived from b and $a/R_\star$. The redistribution factors A_F have been derived from the distribution of phase curve models sampled during fitting. Although the white noise was treated as a free parameter for each dataset as described in Methods, the quoted χ^2 and BIC values were calculated assuming photon noise to allow direct comparison of the two models.

Parameter	**Unit**	**Sinusoid first-order** $\chi^2 = 1896.6$, $\chi^2_\upsilon = 2.6$ BIC $= 2129.5$	**Sinusoid second-order** $\chi^2 = 1864.9$ $\chi^2_\upsilon = 2.5$ BIC $= 2111.0$
$R_p/R_\star$	–	$0.12190^{+0.00009}_{-0.00008}$	$0.12199^{+0.00009}_{-0.00009}$
$a/R_\star$	–	$3.812^{+0.004}_{-0.003}$	$3.785^{+0.003}_{-0.003}$
b	–	$0.114^{+0.002}_{-0.003}$	$0.175^{+0.002}_{-0.002}$
i	degree	$88.29^{+0.05}_{-0.04}$	$87.35^{+0.03}_{-0.02}$
$T_{p,1}$	JD_{UTC}	$2458191.114061^{+0.000049}_{-0.000050}$	$2458191.114045^{+0.000054}_{-0.000048}$
$T_{p,2}$	JD_{UTC}	$2458518.768537^{+0.000073}_{-0.000065}$	$2458518.768609^{+0.000072}_{-0.000060}$
c_0	ppm	18^{+28}_{-14}	26^{+34}_{-19}
c_1	ppm	1195^{+23}_{-29}	1158^{+28}_{-40}
c_2	radian	$3.06^{+0.04}_{-0.05}$	$3.03^{+0.03}_{-0.04}$
c_3	ppm	–	69^{+23}_{-23}
c_4	radian	–	$4.54^{+0.03}_{-0.02}$
ε_0	percent	$1.1^{+1.6}_{-0.8}$	$1.6^{+2.3}_{-1.2}$
A_F	percent	98.6 ± 1.9	95.1 ± 2.5
P	day	1.2749247646 (fixed)	
e	–	0 (fixed)	
u_1	–	0.072 (fixed)	
u_2	–	0.301 (fixed)	

Extended Data Table 2. Results of ATMO "2x PT" retrieval analyses. Values listed are the posterior medians, with uncertainties giving the 1σ credible ranges. First row gives the results of the retrieval analysis performed for the dayside emission spectrum, with metallicity ([M/H]) fitted as a free parameter. Based on the retrieved metallicity for the dayside spectrum, the metallicity was held fixed to [M/H]=0.7 (i.e. 5x solar) for all other orbital phases. Last row gives the results of an additional retrieval performed as a check for phase ϕ=0.95 with [M/H] treated as a free parameter.

ϕ	κ_{IR} (cm^2.g^{-1})	γ_1	Ψ	[M/H] (dex)
Dayside	$-1.78^{+0.08}_{-0.26}$	$1.76^{+0.16}_{-0.30}$	$1.22^{+0.01}_{-0.01}$	$0.76^{+0.30}_{-0.62}$
0.05	$-2.99^{+1.19}_{-0.99}$	$-0.52^{+2.26}_{-2.16}$	$0.30^{+0.18}_{-0.15}$	0.7 (fixed)
0.12	$-2.09^{+0.91}_{-1.31}$	$-1.48^{+2.09}_{-1.54}$	$0.62^{+0.09}_{-0.14}$	0.7 (fixed)
0.17	$2.59^{+1.24}_{-1.36}$	$-1.09^{+1.45}_{-1.65}$	$0.73^{+0.06}_{-0.11}$	0.7 (fixed)
0.23	$-2.33^{+0.98}_{-1.83}$	$-0.52^{+3.00}_{-2.03}$	$0.64^{+0.11}_{-0.21}$	0.7 (fixed)
0.28	$-2.05^{+0.91}_{-1.82}$	$-0.72^{+3.19}_{-1.64}$	$0.73^{+0.09}_{-0.21}$	0.7 (fixed)
0.32	$-2.32^{+0.71}_{-0.45}$	$3.28^{+0.43}_{-2.85}$	$1.31^{+0.04}_{-0.05}$	0.7 (fixed)
0.38	$-2.17^{+0.47}_{-0.34}$	$3.29^{+0.40}_{-1.48}$	$1.30^{+0.02}_{-0.05}$	0.7 (fixed)
0.43	$-1.75^{+0.11}_{-0.14}$	$1.64^{+0.09}_{-0.13}$	$1.25^{+0.03}_{-0.03}$	0.7 (fixed)
0.57	$-2.04^{+0.34}_{-0.44}$	$3.11^{+0.50}_{-1.27}$	$1.27^{+0.02}_{-0.04}$	0.7 (fixed)
0.62	$-1.78^{+0.18}_{-0.16}$	$1.79^{+0.12}_{-0.14}$	$1.22^{+0.05}_{-0.04}$	0.7 (fixed)
0.68	$-2.77^{+1.17}_{-1.80}$	$0.20^{+0.71}_{-0.49}$	$1.13^{+0.19}_{-0.14}$	0.7 (fixed)
0.72	$-2.61^{+1.01}_{-1.32}$	$-0.99^{+2.64}_{-1.66}$	$0.40^{+0.18}_{-0.21}$	0.7 (fixed)
0.78	$-2.55^{+1.32}_{-1.72}$	$-0.86^{+3.51}_{-1.75}$	$0.70^{+0.08}_{-0.14}$	0.7 (fixed)
0.82	$-2.67^{+1.45}_{-1.62}$	$-1.23^{+2.32}_{-1.65}$	$0.69^{+0.07}_{-0.14}$	0.7 (fixed)
0.88	$-1.88^{+0.53}_{-0.62}$	$-1.83^{+1.21}_{-1.10}$	$0.71^{+0.06}_{-0.08}$	0.7 (fixed)
0.95	$-1.89^{+0.56}_{-0.56}$	$-1.90^{+1.24}_{-1.13}$	$0.70^{+0.06}_{-0.08}$	0.7 (fixed)
0.95 (free [M/H])	$-1.76^{+0.54}_{-0.92}$	$-1.82^{+0.98}_{-1.30}$	$0.70^{+0.06}_{-0.10}$	$0.66^{+0.70}_{-1.02}$

Extended Data Table 3. Astrophysical parameters obtained from the spectroscopic phase curve fits with the hot spot phase (c_2) and higher-order terms (c_3, c_4) allowed to vary as free parameters. Same format as Extended Data Tables 1 and 2.

λ (μm)	u_1	u_2	R_p/R_s	c_0 (ppm)	c_1 (ppm)	c_2 (radian)	c_3 (ppm)	c_4 (radian)	χ^2_v	BIC
1.137-1.179	0.126	0.290	$0.1209^{+0.00018}_{-0.00018}$	25^{+33}_{-18}	980^{+41}_{-48}	$3.18^{+0.09}_{-0.09}$	72^{+38}_{-36}	$4.91^{+0.06}_{-0.06}$	1.2	1037.3
1.179-1.220	0.115	0.293	$0.12119^{+0.00017}_{-0.00017}$	36^{+47}_{-26}	972^{+46}_{-52}	$2.95^{+0.10}_{-0.09}$	51^{+35}_{-30}	$3.68^{+0.44}_{-0.41}$	1.2	993.0
1.220-1.262	0.105	0.298	$0.12096^{+0.00017}_{-0.00016}$	31^{+43}_{-23}	985^{+45}_{-52}	$3.05^{+0.11}_{-0.10}$	75^{+32}_{-34}	$3.93^{+0.16}_{-0.11}$	1.1	937.7
1.262-1.304	0.074	0.310	$0.12104^{+0.00019}_{-0.00017}$	94^{+73}_{-61}	968^{+71}_{-84}	$2.91^{+0.12}_{-0.10}$	81^{+39}_{-37}	$4.09^{+0.17}_{-0.15}$	1.3	1069.1
1.304-1.345	0.086	0.303	$0.1204^{+0.00017}_{-0.00017}$	183^{+72}_{-79}	887^{+84}_{-79}	$3.16^{+0.14}_{-0.15}$	110^{+34}_{-32}	$4.16^{+0.15}_{-0.14}$	1.2	1012.6
1.345-1.387	0.076	0.304	$0.12096^{+0.00016}_{-0.00016}$	50^{+56}_{-34}	1204^{+50}_{-63}	$2.96^{+0.09}_{-0.08}$	113^{+34}_{-33}	$4.05^{+0.20}_{-0.22}$	1.1	906.0
1.387-1.429	0.067	0.305	$0.12097^{+0.00018}_{-0.00019}$	48^{+54}_{-34}	1227^{+47}_{-60}	$3.18^{+0.08}_{-0.07}$	132^{+37}_{-40}	$4.21^{+0.08}_{-0.09}$	1.2	1005.2
1.429-1.470	0.056	0.306	$0.12150^{+0.00019}_{-0.00017}$	33^{+47}_{-25}	1336^{+49}_{-54}	$3.04^{+0.07}_{-0.08}$	94^{+37}_{-36}	$4.54^{+0.10}_{-0.10}$	1.1	965.4
1.470-1.512	0.047	0.306	$0.12152^{+0.00017}_{-0.00018}$	129^{+83}_{-74}	1207^{+84}_{-87}	$3.10^{+0.11}_{-0.11}$	79^{+35}_{-34}	$3.78^{+0.15}_{-0.17}$	1.2	996.7
1.512-1.553	0.039	0.302	$0.12109^{+0.00020}_{-0.00017}$	39^{+49}_{-29}	1303^{+49}_{-57}	$3.03^{+0.09}_{-0.06}$	43^{+36}_{-27}	$3.98^{+0.13}_{-0.16}$	1.2	1008.8
1.553-1.595	0.030	0.298	$0.12165^{+0.00020}_{-0.00020}$	25^{+40}_{-19}	1340^{+49}_{-55}	$3.04^{+0.10}_{-0.09}$	152^{+45}_{-45}	$5.23^{+0.07}_{-0.08}$	1.2	1019.6
1.595-1.637	0.024	0.300	$0.12088^{+0.00021}_{-0.00022}$	47^{+64}_{-34}	1318^{+66}_{-71}	$3.14^{+0.12}_{-0.11}$	108^{+49}_{-47}	$4.54^{+0.12}_{-0.10}$	1.4	1171.0

Extended Data Table 4. Astrophysical parameters obtained from the spectroscopic phase curve fits with the hot spot phase (c_2) and higher-order terms (c_3, c_4) held fixed to the values determined for the broadband light curve. Same format as Extended Data Tables 1-3.

λ (μm)	u_1	u_2	R_p/R_s	c_0 (ppm)	c_1 (ppm)	χ^2_v	BIC
1.137-1.179	0.126	0.290	$0.12108^{+0.00016}_{-0.00015}$	24^{+31}_{-17}	990^{+36}_{-41}	1.2	1020.6
1.179-1.220	0.115	0.293	$0.12132^{+0.00015}_{-0.00016}$	29^{+41}_{-21}	971^{+36}_{-45}	1.2	977.1
1.220-1.262	0.105	0.298	$0.12111^{+0.00015}_{-0.00014}$	24^{+38}_{-17}	1004^{+35}_{-42}	1.1	921.5
1.262-1.304	0.074	0.310	$0.12115^{+0.00017}_{-0.00017}$	82^{+66}_{-52}	979^{+57}_{-67}	1.3	1055.2
1.304-1.345	0.086	0.303	$0.12115^{+0.00016}_{-0.00016}$	154^{+72}_{-71}	947^{+75}_{-76}	1.2	1001.7
1.345-1.387	0.076	0.304	$0.12112^{+0.00015}_{-0.00015}$	49^{+55}_{-34}	1229^{+44}_{-58}	1.1	897.0
1.387-1.429	0.067	0.305	$0.12113^{+0.00016}_{-0.00016}$	38^{+45}_{-27}	1281^{+41}_{-51}	1.2	999.9
1.429-1.470	0.056	0.306	$0.12154^{+0.00016}_{-0.00016}$	28^{+39}_{-20}	1363^{+38}_{-46}	1.1	949.3
1.470-1.512	0.047	0.306	$0.12165^{+0.00018}_{-0.00017}$	95^{+67}_{-59}	1255^{+64}_{-75}	1.2	985.7
1.512-1.553	0.039	0.302	$0.12121^{+0.00016}_{-0.00018}$	28^{+44}_{-21}	1302^{+43}_{-47}	1.2	992.0
1.553-1.595	0.030	0.298	$0.12148^{+0.00018}_{-0.00018}$	36^{+48}_{-26}	1382^{+44}_{-59}	1.2	1004.8
1.595-1.637	0.024	0.300	$0.12095^{+0.00020}_{-0.00023}$	48^{+56}_{-34}	1354^{+56}_{-67}	1.4	1155.9

Extended Data Table 5. Heat redistribution factors and fit metrics for the two suites of spectroscopic light curve fits. Heat redistribution factors A_F were derived in the same manner as described for Extended Data Table 1. Fit metrics have been reproduced here from Extended Data Tables 3 and 4 to ease comparison between the two suites of phase curve fits.

	c_2, c_3, c_4 allowed to vary			**c_2, c_3, c_4 held fixed**		
λ (μm)	**A_F (%)**	**χ^2_v**	**BIC**	**A_F (%)**	**χ^2_v**	**BIC**
1.137-1.179	94.1 ± 3.1	1.2	1037.3	93.5 ± 2.6	1.2	1020.6
1.179-1.220	95.2 ± 3.8	1.2	993.0	92.9 ± 2.9	1.2	977.1
1.220-1.262	95.4 ± 3.4	1.1	937.7	93.5 ± 3.0	1.1	921.5
1.262-1.304	88.9 ± 5.7	1.3	1069.14	88.7 ± 5.0	1.3	1055.2
1.304-1.345	81.8 ± 6.6	1.2	1012.6	82.8 ± 6.0	1.2	1001.7
1.345-1.387	93.7 ± 3.4	1.1	906.0	92.9 ± 3.4	1.1	897.0
1.387-1.429	94.7 ± 3.3	1.2	1005.2	93.9 ± 2.8	1.2	999.9
1.429-1.470	94.6 ± 2.6	1.1	965.4	94.9 ± 2.1	1.2	949.3
1.470-1.512	90.0 ± 5.5	1.2	996.7	89.9 ± 4.3	1.2	985.7
1.512-1.553	96.4 ± 2.9	1.2	1008.8	94.6 ± 2.5	1.4	992.0
1.553-1.595	90.6 ± 2.8	1.2	1019.6	94.4 ± 2.7	1.2	1004.8
1.595-1.637	94.0 ± 3.6	1.4	1171.0	93.5 ± 3.2	1.2	1155.9

Extended Data Table 6. Measured planetary emission spectrum at each orbital phase. Values are in units of ppm and quoted uncertainties give the 1σ credible ranges. *Continued on next page.*

	Spectroscopic wavelength channel (micron)					
ϕ	**1.137-1.179**	**1.179-1.220**	**1.220-1.262**	**1.262-1.304**	**1.304-1.345**	**1.345-1.387**
0.05	28 ± 52	68 ± 60	30 ± 47	71 ± 48	201 ± 54	70 ± 48
0.12	182 ± 51	228 ± 63	234 ± 50	387 ± 57	313 ± 56	310 ± 56
0.17	425 ± 53	420 ± 58	369 ± 50	437 ± 54	475 ± 56	472 ± 59
0.23	605 ± 59	539 ± 64	526 ± 56	594 ± 51	738 ± 54	659 ± 48
0.28	705 ± 65	665 ± 55	758 ± 53	762 ± 48	804 ± 50	891 ± 48
0.32	861 ± 49	900 ± 61	851 ± 48	892 ± 51	1004 ± 48	1053 ± 48
0.38	909 ± 48	975 ± 52	1005 ± 45	1066 ± 46	1088 ± 49	1266 ± 45
0.43	1087 ± 46	1011 ± 53	1040 ± 46	1086 ± 45	1092 ± 49	1282 ± 45
0.57	984 ± 48	948 ± 57	934 ± 44	958 ± 46	1034 ± 46	1133 ± 44
0.62	813 ± 54	815 ± 54	829 ± 45	843 ± 45	895 ± 48	1018 ± 48
0.68	594 ± 57	588 ± 53	636 ± 50	781 ± 52	731 ± 58	833 ± 59
0.72	508 ± 57	525 ± 56	537 ± 54	577 ± 51	679 ± 51	688 ± 53
0.78	360 ± 53	382 ± 67	401 ± 53	479 ± 60	495 ± 53	493 ± 45
0.82	233 ± 55	297 ± 65	268 ± 50	292 ± 48	388 ± 61	325 ± 51
0.88	226 ± 61	115 ± 57	161 ± 46	243 ± 59	335 ± 55	136 ± 54
0.95	82 ± 49	48 ± 54	93 ± 45	162 ± 50	219 ± 47	86 ± 47

Extended Data Table 6 (*continued from previous page)*.

	Spectroscopic wavelength channel (micron)					
ϕ	**1.387-1.429**	**1.429-1.470**	**1.470-1.512**	**1.512-1.553**	**1.553-1.595**	**1.595-1.637**
0.05	45 ± 60	56 ± 52	169 ± 54	50 ± 57	78 ± 62	19 ± 71
0.12	253 ± 60	321 ± 50	327 ± 52	304 ± 58	309 ± 60	257 ± 87
0.17	495 ± 58	514 ± 41	524 ± 51	542 ± 64	523 ± 70	568 ± 73
0.23	772 ± 61	752 ± 50	815 ± 52	704 ± 55	746 ± 67	715 ± 69
0.28	894 ± 57	971 ± 47	968 ± 58	936 ± 65	913 ± 68	1078 ± 66
0.32	1169 ± 68	1133 ± 55	1194 ± 57	1113 ± 64	1173 ± 63	1160 ± 71
0.38	1234 ± 58	1336 ± 45	1243 ± 47	1241 ± 56	1351 ± 56	1253 ± 69
0.43	1325 ± 54	1442 ± 45	1383 ± 44	1361 ± 53	1500 ± 60	1477 ± 67
0.57	1209 ± 56	1277 ± 44	1233 ± 44	1188 ± 53	1322 ± 56	1253 ± 66
0.62	980 ± 57	1114 ± 45	1099 ± 46	1106 ± 55	1094 ± 54	1136 ± 65
0.68	935 ± 59	880 ± 48	935 ± 55	878 ± 58	962 ± 55	893 ± 74
0.72	681 ± 59	723 ± 51	708 ± 54	611 ± 59	670 ± 70	708 ± 61
0.78	479 ± 59	528 ± 51	530 ± 55	482 ± 60	475 ± 61	461 ± 78
0.82	272 ± 64	327 ± 57	42 ± 56	403 ± 55	301 ± 61	394 ± 76
0.88	254 ± 61	190 ± 51	226 ± 56	124 ± 57	239 ± 65	219 ± 74
0.95	89 ± 56	86 ± 46	116 ± 50	74 ± 55	121 ± 59	125 ± 69

Extended Data Table 7. Dayside emission spectrum derived from the distribution of phase curve maxima. Quoted values were derived from the distribution of phase curve maxima sampled during spectroscopic phase curve fitting with quoted uncertainties corresponding to the 1σ credible ranges.

λ (μm)	Emission (ppm)
1.137-1.179	1017 ± 29
1.179-1.220	1005 ± 30
1.220-1.262	1033 ± 27
1.262-1.304	1062 ± 29
1.304-1.345	1100 ± 27
1.345-1.387	1281 ± 28
1.387-1.429	1323 ± 30
1.429-1.470	1396 ± 30
1.470-1.512	1349 ± 32
1.512-1.553	1338 ± 33
1.553-1.595	1422 ± 32
1.595-1.637	1408 ± 39

Extended Data Table 8. Emission spectrum χ^2 fit statistics at each orbital phase for the ATMO "2x PT" retrievals, NEMESIS "2x PT" retrievals, and blackbody fits. As described in Methods, the ATMO retrievals assumed chemical equilibrium, the NEMESIS retrievals assumed no constraints for the atmospheric chemistry, and the blackbody fits assumed the planet radiates isothermally. Inferred brightness temperatures with 1σ uncertainties are also reported for the blackbody fits in the last column.

	ATMO 2x PT ($\upsilon = 9$) Equilibrium chemistry 5x solar		**NEMESIS 2x PT ($\upsilon = 6$)** Unconstrained chemistry		**Blackbody ($\upsilon = 11$)** Isothermal radiation		
ϕ	χ^2	χ^2_υ	χ^2	χ^2_υ	χ^2	χ^2_υ	T_b **(Kelvin)**
0.05	11.4	1.3	11.5	2.3	13.8	1.3	1555 ± 52
0.12	7.3	0.8	13.3	2.7	19.7	1.8	1972 ± 22
0.17	2.8	0.3	5.3	1.1	16.9	1.5	2190 ± 16
0.23	9.2	1.0	13.2	2.6	30.8	2.8	2366 ± 13
0.28	4.5	0.5	14.0	2.8	15.5	1.4	2505 ± 11
0.32	4.3	0.5	12.2	2.4	23.1	2.1	2622 ± 10
0.38	9.5	1.1	12.1	2.4	35.1	3.2	2699 ± 9
0.43	11.7	1.3	19.8	4.0	25.6	2.3	2749 ± 8
0.57	8.1	0.9	19.2	3.8	31.4	2.9	2670 ± 9
0.62	3.7	0.4	12.6	2.5	20.5	1.9	2580 ± 9
0.68	7.0	0.8	10.5	2.1	16.1	1.5	2461 ± 12
0.72	8.1	0.9	9.6	1.9	32.1	2.9	2331 ± 13
0.78	4.0	0.4	3.6	0.7	25.6	2.3	2178 ± 16
0.82	7.8	0.9	9.1	1.8	16.0	1.5	2022 ± 20
0.88	15.1	1.7	14.2	2.8	26.5	2.4	1838 ± 28
0.95	7.5	0.8	7.6	1.5	16.0	1.5	1651 ± 38
Mean	**7.6**	**0.8**	**11.7**	**2.3**	**22.8**	**2.1**	
Median	**7.6**	**0.8**	**12.1**	**2.4**	**21.8**	**2.0**	

Extended Data Table 9. Fit metrics demonstrating nightside emission detection. Results are reported for the fiducial ATMO "2x PT" retrievals assuming chemical equilibrium with 5x solar metallicity at the ten phases for which retrievals were performed for the nightside emission while holding the dayside contribution fixed. Also reported are fit statistics obtained in a similar manner except that the nightside emission was fixed to zero (i.e. $\Phi_n = 0$). The Bayes factors reported in the final column are computed as exp(−ΔBIC/2). The final row gives values for the ensemble of phase-resolved emission spectra listed in this table.

	ATMO 2x PT ($\upsilon = 9$) Fiducial model i.e. nonzero nightside emission allowed		**ATMO 2x PT ($\upsilon = 12$)** Fiducial model for dayside contribution but nightside emission fixed to zero		**Model comparison** Favouring nightside emission	
ϕ	χ^2	**BIC**	χ^2	**BIC**	**ΔBIC**	**Bayes Factor**
0.05	11.4	18.8	11.6	11.6	7.2	0.03
0.12	7.3	14.8	17.3	17.3	−2.5	3.5
0.17	2.8	10.3	20.8	20.8	−10.5	193.6
0.23	9.2	16.7	17.9	17.9	−1.3	1.9
0.28	4.5	12.0	11.5	11.5	0.5	0.8
0.72	8.1	15.6	8.5	8.5	7.1	0.03
0.78	4.0	11.4	20.6	20.6	−9.1	96.9
0.82	7.8	15.2	20.7	20.7	−5.5	15.7
0.88	15.1	22.5	50.1	50.1	−27.6	9.9×10^5
0.95	7.5	15.0	57.5	57.5	−42.5	1.7×10^9
All ϕ	**77.7**	**221.3**	**236.5**	**380.1**	**−158.8**	**3.0×10^{34}**